Study of the irreducible background for the X$\rightarrow$ WZ $\rightarrow \ell\ \nu\ \ell\ell$ resonance search performed in ATLAS at 13 TeV

Masterarbeit
zur Erlangung des Hochschulgrades
Master of Science
im Master-Studiengang Physik

vorgelegt von

Alhawiti, Fawaz Mutlaq S
geboren am 22.05.1992 in Tabouk (Saudi-Arabien)

Institut für Kern- und Teilchenphysik
Fakultät Physik
Bereich Mathematik und Naturwissenschaften
Technische Universität Dresden
2021

Eingereicht am 23. September 2021

1. Gutachter: Dr. Frank Siegert
2. Gutachter: Prof. Dr. Arno Straessner

Acknowledgements

First of all, I am grateful to God for blessing me with all the great people around me. I would like to thank the government of Saudi Arabia for giving me the opportunity to study in Germany and covering my study and living expenses during these years.

I am also thankful to the TU-Dresden and all its members for their helpful and careful guidance. I also must not forget to thank all members of the VBS-Dresden group, especially Prof. Dr. Michael Kobel, Dr. Frank Siegert, Dr. Joany Manjarrés, Carsten Bittrich and Abhishek Nag. A very special thank you to my supervisor Dr. Joany Manjarrés for her advice, guidance and massive support during this research.

Finally, I would like to say a warm thank you to my family, my friends and my English teacher Alice, without your help and guidance this thesis would have not been the same.

Abstract

Zusammenfassung

Es besteht die Notwendigkeit, die Fragen zu beantworten, die das Standardmodell SM nicht erklären kann. Es werden verschiedene Strategien angewandt, um nach neuer Physik jenseits des SM zu suchen und die fehlenden Antworten zu erhalten. Die Resonanzsuche ist eine direkte Untersuchung von unbekannten Erhebungen über einem ansonsten gut bekannten Untergrund in den Spektren der invarianten Masse, die neue Teilchen darstellen könnten. Dieses Dokument konzentriert sich auf die Untersuchung des nicht-reduzierbaren Untergrunds für die X$\rightarrow$ WZ $\rightarrow \ell\ \nu\ \ell\ell$ Resonanzsuche, die in ATLAS bei 13 TeV durchgeführt wurde. Die Daten wurden von ATLAS während des gesamten Laufs 2 (2015-2018) gesammelt.

In dieser Arbeit wird die Modellierung des Hauptuntergrundes für die WZ-Resonanzsuche betrachtet, insbesondere in einer Topologie, die Vektor-Bosonen-Fusion (VBF) genannt wird. Der Hauptbeitrag zur WZ-Produktion ist der WZ-QCD-Prozess. Dies bietet die Möglichkeit, die WZ-QCD-Produktion in der VBF-Kontrollregion eingehend zu untersuchen und zu optimieren. Ein Teil dieser Arbeit konzentriert sich auch auf einen Vergleich zwischen zwei verschiedenen Monte-Carlo-Generatoren, welche die WZ-Produktion simulieren können.

Abstract

There is a need to answer the questions that the Standard Model theory SM fails to explain. Various strategies are used to look for new physics beyond the SM and obtain the missing answers. The resonance search is a direct investigation of unexpected bumps over an otherwise well known background in the invariant mass spectra, those bumps might represent new particles. This document focuses on the study of the irreducible background for the X$\rightarrow$ WZ $\rightarrow \ell\ \nu\ \ell\ell$ resonance search performed in ATLAS at 13 TeV. The data was collected by ATLAS during the full Run 2 (2015-2018).

In this thesis the modelling of the main background for the WZ resonance search is considered, in particular in a topology called the Vector Boson Fusion (VBF). The main contribution to the WZ production is the WZ QCD. This creates an opportunity to perform a deep study and optimization of WZ QCD production in the VBF control region. A part of this thesis also focuses on a comparison between two different Monte Carlo generators which can carry out the WZ production.

Contents

1 Introduction

Particle physics is a revolutionary branch of physics that aims to fully understand the building blocks of the universe, from their creation and development to their interactions and annihilation. Over the last century, tangible advancements in this area of physics have been made by numerous theoretical and experimental physicists, such as discovery and identification of new fundamental particles and the development of a successful comprehensive theory called the Standard Model of particle physics (abbreviated as SM).

The SM theory is a successful theory of particle physics that describes all fundamental forces (electromagnetic, weak and strong) except gravity. Moreover, it has precisely predicted various new particles such as both W and Z bosons and the Higgs boson. With the addition of the Higgs boson, which was observed in 2012 by the ATLAS and CMS collaborations at CERN, the whole picture of the SM blocks appears to be complete. Nonetheless, the SM cannot provide answers for a wealth of questions, such as the question of the neutrino mass. Dark matter and dark energy largely remain a mystery, and a way to unify all the forces of nature has yet to be discovered [34].

Nowadays, physicists earnestly attempt to take a look beyond the SM, hoping to obtain the answers that could satisfy their goals. Various approaches are being taken to understand the SM deeper and possibly observe new physics. According to recent research, one of the most effective approaches is studying the predicted interactions of the SM particles in different topologies. Most of the work in this thesis is done in a topology called the vector boson fusion (VBF). It is going to be described in detail in chapter 2.6.1.

This thesis focuses on the study of the irreducible background for the X$\rightarrow$ WZ $\rightarrow \ell\ \nu\ \ell\ell$ resonance search performed in ATLAS at 13 TeV. Only the leptonic final states of the WZ diboson production will be considered, with ℓ refers to an electron or a muon. The search for WZ resonances is a crucial investigation that leads to a deeper understanding of the electroweak symmetry breaking (EWSB), and could also point to the evidence of new physics. It is worth mentioning that there are a multitude of theories that address vector diboson resonances at high energy scales, such as the Technicolour [23, 11] and Little Higgs models [7]. Two models will be considered in this thesis: the Heavy Vector Triplet HVT and the Georgi-Machacek (MG), which are described in chapter 2.3.1 and 2.3.2, respectively.

2 Theoretical Framework

2.1 The Standard Model of Particle Physics

The goal of particle physics is to understand the universe from the Big Bang, the creation of the first protons and the development of galaxies, planets, etc., to the present era. It has been discovered that everything in our universe is made from basic fundamental particles. These particles interact with each other, controlled by four fundamental forces. Many theories were created in attempts to describe the results of the experiments and understand how the particles behave and why they do it in such ways.
The Standard Model of Particle Physics is a theory that best describes the three fundamental forces (the electromagnetic force, the weak and strong interactions) at the elementary particle level. It is the best theory to date. The fourth one, gravity, is not included in the SM because it is too weak to be considered at the current scale of particle physics. Gravity, along with dark matter and dark energy, cannot be described by the Standard Model. These four known forces together with their properties are listed in tabel 2.1. This model has been in development between 1961-1973.

Force	Strengh	Boson	Mass/GeV
Strong	1	Gluon	0
Electromagntesim	10^{-3}	Photon	0
Weak	10^{-8}	$W^{\pm}$/Z	80.4/91.2
Gravity	10^{-37}	Graviton?	0

Table 2.1: The List of fundamental forces of nature with their properties (strength- associated Boson-mass). [34]

The Standard Model is a gauge Quantum Field theory, based on the local gauge symmetry group $SU(3)_C \otimes SU(2)_L \otimes U(1)_Y$. The SM is invariant under rotation in flavour space SU(2), invariant under local gauge transformation U(1) and invariant under rotation in colour space SU(3). According to Noether's theorem [29], each invariance under local symmetry has a corresponding conservation law. In this case, colour charge, weak isospin T_3, electric charge Q and weak hypercharge Y are conserved quantities.
The Standard Model (SM) of particle physics provides a great description of all observed fundamental particles and their interaction in nature. These particles are illustrated in figure 2.1. The last two particles discovered were the neutrino in 2000 and the Higgs boson in 2012.

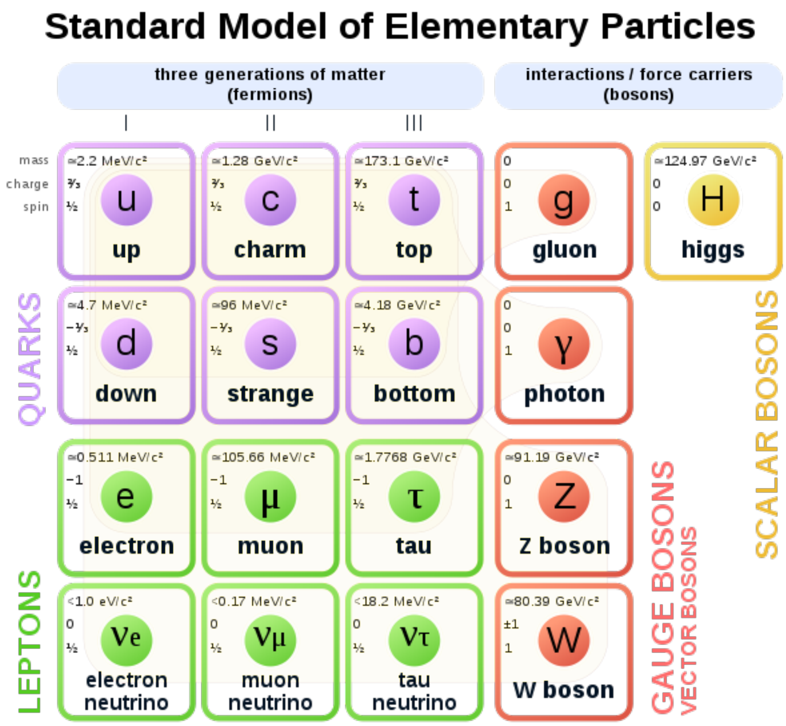

Figure 2.1: The Standard Model table of elementary particles with their properties (mass-charge-spin). [15]

These fundamental particles are separated into categories. The first one is called fermions. They obey Fermi-Dirac statistics and have half integral spin quantum numbers ($\frac{1}{2}$, $\frac{2}{3}$, ...). They occur in two types called quarks and leptons. Each type has six flavours. Flavours of quarks are up, down, charm, strange, top and bottom. Quarks come in three different generations, the first generation contains up and down quarks, they make up all stable matter in the universe. The second and third generations contain charm and strange, and top and bottom, respectively. The quarks interact via electromagnetic, weak and strong forces. The second type of fermions is Leptons, they are e^-, μ^-, τ^-, ν_e, ν_μ and ν_τ. Also the six leptons are also arranged in three generations [e^-,ν_e], [μ^-,ν_μ], [τ^-,ν_τ]. The leptons do not interact via strong force, only via weak and electromagnetic force. The e^- μ^- τ^- have charge and mass, but neutrinos have natural charge and a very small mass.

The second major group of the SM is bosons. They obey Bose–Einstein statistics and have integer spins (expressed as spin quantum numbers such as 0, 1, 2, ...). Each force in nature is carried by the corresponding boson: the electromagnetic force is carried by the photon γ , the strong force carried by the gluon g and the weak force carried by the $W^{\pm}$/Z bosons. The last particle is the Higgs boson. The Higgs mechanism explains why some particles have mass and others do not. For further explanation of the Standard Model of particles, see [1].

The SM is not a single theory, but several theories combined. The Quantum electrodynamics (QED) theory, developed in 1930, describes the interaction of light with matter. The exchange particle responsible for the electromagnetic force is called the gauge photon. QED is a gauge theory with a special local U(1) symmetry. The Lagrangian of the QED is described by the equation 2.1.

$$\begin{aligned} L_{QED} &= L_e + L_{Maxwell} + L_{interact} \\ &= \bar{\psi}(i\gamma^\mu \partial_\mu - m)\psi - \frac{1}{4}F_{\mu\nu}F^{\mu\nu} + e\bar{\psi}\gamma^\mu Q A_\mu \psi \end{aligned} \tag{2.1}$$

where ψ is the Dirac wave-function of e^- or e^+. A_μ is the electromagnetic vector potential, $F_{\mu\nu}$ is the electromagnetic field tensor and $e\bar{\psi}\gamma^\mu Q A_\mu \psi$ is the semiclassical coupling of electrons to the electromagnetic field.

Furthermore, there is a part of SM that deals with the strong interaction described by a gauge theory called Quantum chromodynamics (QCD), developed in 1973, with symmetry group SU(3). In the strong force, gluons are responsible for binding quarks together. The QCD Lagrangian is:

$$\begin{aligned} &L_{QCD} = -\frac{1}{4}F^a_{\mu\nu}F^{\mu\nu}_a + \sum_{f=1}^{6} \bar{\psi}_{f,i}(i\gamma^\mu D^{ij}_\mu - m_f \delta_{ij})\psi_{f,j} \\ &F^a_{\mu\nu} = \partial_\mu A^a_\nu - \partial_\nu A^a_\mu + g_o f_{abc} A^b_\mu A^c_\nu \\ &D_\mu = \partial_\mu - i g_o A^a_\mu T_a \end{aligned} \tag{2.2}$$

where [a=1,....,8 ; i=1,2,3].

In QED, photons cannot interact since they do not have a charge, but in QCD, gluons can interact since gluons have a colour charge. QED is a abelian theory, whereas QCD is a nonabelian theory [35]. Despite the fact that the Standard Model is the current best description of the fundamental world, it still has deficiencies and cannot explain all physical aspects of the universe. Moreover, many questions do not have any answers, such as: What is dark matter? What happened to the antimatter after the Big Bang? Are quarks and leptons truly fundamental? and more.

2.2 Electroweak Symmetry Breaking

According to the Grand Unified theory (GUT), which was proposed by a number of physicists, all the forces in nature are merged into one force at high energies. In the present low energy universe the weak and electromagnetic forces are different, compared to the high energy state of the universe in the first few seconds after the Big Bang. The electromagnetic interactions are described by the QFT, which is a specialization of QED Quantum Electrodynamics (see section 2.1)

In the weak theory, which can also be called Quantum Flavour Dynamics (QFD), the force carriers in weak interactions are spin-1 bosons (W^+, W^-, Z), which couple to quarks and leptons based on local gauge symmetry $SU(2)_I$, where I is the weak isospin. The weak force violates parity P, charge conjunction C, and CP-symmetry, while the CPT symmetry is still conserved [10]. Moreover, it is responsible for changing the flavour of particles.

The electroweak theory describes the electroweak force, which is the unification of the electromagnetic and weak forces. In 1979, a Nobel Prize in physics was awarded to physicists Sheldon Glashow, Abdus Salam and Steven Weinberg for their contributions to the unification of the weak and electromagnetic interactions. The total unbroken gauge symmetry group of the SM is

$$SU(3)_C \otimes SU(2)_L \otimes U(1)_Y \tag{2.3}$$

at high energy. The underlying symmetry of the electroweak interaction is $SU(2)_L \otimes U(1)_Y$, where Y is the hypercharge

$$Y = 2(Q - I^3), \text{ Q is the electric charge and } I^3 \text{ is the weak isospin} \tag{2.4}$$

The Higgs field is also included in the Weinberg-Salam model (a theory that describes the electroweak interaction). The Higgs mechanism provides a logical explanation of how leptons (e, μ, τ) acquire mass, even though neutrinos are massless. Furthermore, the gauge bosons ($W^{\pm}$, Z^0) acquire mass, despite the fact that the photons are massless. Recent experiments have led to discoveries that suggest that neutrino mass is non-zero. This is evidence of physics beyond the Standard Model. More information about the issues surrounding neutrinos can be found in [36].

Starting with the standard Dirac Lagrangian, with setting m=0

$$L_{Dirac} = i\bar{\psi}\gamma^{\mu}\partial_{\mu}\psi \tag{2.5}$$

The ψ is a Dirac spinor. It is a two-component object:

$$\psi = \begin{pmatrix} \psi_R \\ \psi_L \end{pmatrix} \tag{2.6}$$

The violation of parity in weak interactions provides a way to distinguish between left and right by means of a detailed operational definition. Each component,ψ_R ψ_L, represents the right-handed spinor and the left-handed spinor, respectively. Both spinors are two-component objects. The projection operator $P_{\pm}$ is used to define the chirality states:

$$P_{\pm} = \frac{1}{2}(1 \pm \gamma^5) \quad where \quad P_{+}\psi = \psi_R \quad P_{-}\psi = \psi_L \tag{2.7}$$

γ^5 is the fifth Dirac matrix (see Appendix A.1 for additional information)

For ψ_R:

$$\psi_R = \frac{1}{2}(1+\gamma^5)\psi = \begin{pmatrix} \psi_+ \\ 0 \end{pmatrix} \tag{2.8}$$

and similarly for ψ_L:

$$\psi_L = \frac{1}{2}(1-\gamma^5)\psi = \begin{pmatrix} 0 \\ \psi_- \end{pmatrix} \tag{2.9}$$

Now the Dirac field can be written as:

$$\psi = \begin{pmatrix} \psi_R \\ \psi_L \end{pmatrix} = \begin{pmatrix} 0 \\ \psi_L \end{pmatrix} + \begin{pmatrix} \psi_R \\ 0 \end{pmatrix} = \psi_R + \psi_L \tag{2.10}$$

Then the equation 2.5 can be written as:

$$L_{Dirac} = i\bar{\psi_R}\gamma^\mu\partial_\mu\psi_R + i\bar{\psi_L}\gamma^\mu\partial_\mu\psi_L \tag{2.11}$$

The equation 2.11 describes 4-component objects with left-right chirality. Seeing as the weak force affects only left-chiral particles but not the right-chiral ones, as well as right-chiral antiparticles but not the left-chiral antiparticles, the fermions are treated differently in weak sector by using a singlet notation for the right component ψ_R, and a doublet notation for the left component ψ_L fields:

$$\psi_L = \begin{pmatrix} \nu_e \\ e \end{pmatrix}_L, \begin{pmatrix} \nu_\mu \\ \mu \end{pmatrix}_L, \begin{pmatrix} \nu_\tau \\ \tau \end{pmatrix}_L, \begin{pmatrix} u \\ d \end{pmatrix}_L, \begin{pmatrix} c \\ s \end{pmatrix}_L, \begin{pmatrix} t \\ b \end{pmatrix}_L \tag{2.12}$$

$$\psi_R = e_R, \mu_R, \tau_R, c_R, s_R, t_R, b_R \tag{2.13}$$

Focusing on first generation of leptons $\psi_L = \begin{pmatrix} \nu_e \\ e \end{pmatrix}_L$, $\psi_R = e_R$ and considering that the muon and tau are simply heavier duplicates of the electron, the equation can be written as:

$$L_{Dirac} = i\bar{\psi_R}\gamma^\mu\partial_\mu\psi_R + i\bar{\psi_R}\gamma^\mu\partial_\mu\psi_R \tag{2.14}$$

describing the Dirac fields of the electroweak interaction, considering only electrons. Muon and tau are also considered in the full theory of leptons. In addition to this, there are three types of charge that are present during electroweak interaction: the electric charge Q, the weak isospin I, and the weak hypercharge Y. These charges are related according to the Gell-Mann-Nishijima formula 2.4.

As mentioned earlier, the electroweak sector includes a combination of two gauge symmetry groups $SU(2)_L \otimes U(1)_Y$. The $SU(2)$ generates three gauge bosons: W^1_μ W^2_μ W^3_μ. The $U(1)$ generates one gauge boson: B_μ. However, after the gauge fields are included, the total Lagrangian consists of two parts:

$$L_{total} = L_{leptons} + L_{gauge}$$

Mathematically, the local gauge invariance requires the Lagrangian density to be invariant under a gauge transformation. The U(1) transformation on the left-right handed spinor is shown in the matrix below:

$$\begin{pmatrix} \nu_e \\ e_L \\ e_R \end{pmatrix} \to \begin{pmatrix} \nu_e' \\ e_L' \\ e_R' \end{pmatrix} = \begin{pmatrix} e^{\frac{i\beta}{2}} & 0 & 0 \\ 0 & e^{\frac{i\beta}{2}} & 0 \\ 0 & 0 & e^{i\beta} \end{pmatrix} \begin{pmatrix} \nu_e \\ e_L \\ e_R \end{pmatrix} \tag{2.15}$$

β is a scalar. Similarly, for SU(2), the transformation can be written as:

$$\begin{pmatrix} \nu_e \\ e_L \\ e_R \end{pmatrix} \to \begin{pmatrix} \nu_e' \\ e_L' \\ e_R' \end{pmatrix} = \begin{pmatrix} e^{\frac{-i\tau\alpha}{2}} & 0 & 0 \\ 0 & e^{\frac{-i\tau\alpha}{2}} & 0 \\ 0 & 0 & 1 \end{pmatrix} \begin{pmatrix} \nu_e \\ e_L \\ e_R \end{pmatrix} \tag{2.16}$$

where τ_i are the Pauli matrices.(for more information see Appendix A.1). The Lagrangian is invariant in these transformations. When a kinematic term is added, the gauge field becomes dynamical, by using the formula $F_{\mu\nu} = -\frac{i}{g}[D_\mu, D_\nu]$:

$$\begin{aligned} \text{for } SU(2)_L : F^l_{\mu\nu} &= \partial_\mu W^l_\nu - \partial_\nu W^a_\mu - g_W \epsilon^{lmn} W^m_\mu W^n_\nu \\ \text{for } U(1)_Y : F_{\mu\nu} &= \partial_\mu B_\nu - \partial_\nu B_\mu \\ \partial_\mu &\to \partial_\mu + \frac{ig_B}{2} B_\mu \end{aligned} \tag{2.17}$$

where l=1,2,3 and g_B,g_W are the coupling constants associated with the gauge field B_μ and W^l_μ, respectively. The equation 2.18 shows the total Lagrangian, including the gauge and lepton parts:

$$\begin{aligned} L &= L_{lepton} + L_{gauge} \\ &= i\bar{\psi}_R \gamma^\mu (\partial_\mu + \frac{ig_B}{2} B_\mu)\psi_R + i\bar{\psi}_L \gamma^\mu (\partial_\mu \frac{ig_B}{2} B_\mu + ig_W \frac{\vec{\tau}}{2}.\vec{W}_\mu)\psi_L \\ &-\frac{1}{4} f_{\mu\nu} f^{\mu\nu} - \frac{1}{8} Tr(F_{\mu\nu}F^{\mu\nu}) \end{aligned} \tag{2.18}$$

The coupling constants g_W and g_B are related according to:

$$\tan\theta_W = \frac{g_W}{g_B} \tag{2.19}$$

The angle θ_W is called the weak mixing angle, also known as the Weinberg angle. However, the B_μ mixes with the neutral W_μ^3 to obtain two orthogonal states:

$$\begin{aligned} A_\mu &= B_\mu cos\theta_W + W_\mu^3 sin\theta_W \\ Z_\mu &= -B_\mu cos\theta_W + W_\mu^3 sin\theta_W \end{aligned} \tag{2.20}$$

The gauge field A_μ is the photon field that describes the massless photon particle, related to $U(1)_{EW}$. The Z_μ is the Z gauge field that describes the massive Z boson of the weak interaction. All the steps mentioned above are taken in order to describe a theory of leptons and 4 gauge bosons without mass term, in contrast to the measurements obtained during experiments which suggest that $W^\pm$ and Z bosons are massive. Adding the mass term to the equation 2.18 directly will damage the local gauge invariant. Instead of that, the symmetry breaking methods are used to introduce mass term.

Spontaneous Symmetry Breaking

The following is an approach that includes redefining of the vacuum ground state and then adding a Higgs field as scalar field ϕ, coupled to the gauge bosons:

$$\phi = \begin{pmatrix} \phi^A \\ \phi^B \end{pmatrix} \tag{2.21}$$

It is a 2-component object, where each component is a complex scalar field:

$$\phi^A = \frac{\phi_1 + i\phi_2}{\sqrt{2}}, \quad \phi^B = \frac{\phi_3 + i\phi_4}{\sqrt{2}} \tag{2.22}$$

Now the Lagrangian of the scalar Higgs field is given by

$$L_{Higgs} = (D_\mu\phi)^\dagger(D^\mu\phi) - V(\phi). \tag{2.23}$$

where $(D_\mu\phi)^\dagger(D^\mu\phi)$ are the kinetic energy terms and $V(\phi)$ is the new potential of the Higgs field. The potential can be written as:

$$V(\phi) = \mu^2\phi^\dagger\phi + \lambda(\phi^\dagger\phi)^2 \tag{2.24}$$

$SU(2)_L \otimes U(1)_Y$ is invariant under the Higss potential $V(\phi)$. When $\mu^2 < 0$, the potential energy $V(\phi)$ resembles a Mexican hat in the illustration (see figure 2.2). the minimum of the potential is:

$$\phi^\dagger\phi = -\frac{\mu^2}{2\lambda} = \frac{\nu^2}{2}. \tag{2.25}$$

The vacuum expectation value for the field ϕ can be written as:

$$\langle\phi\rangle = \frac{1}{\sqrt{2}}\begin{pmatrix} 0 \\ \nu \end{pmatrix} \tag{2.26}$$

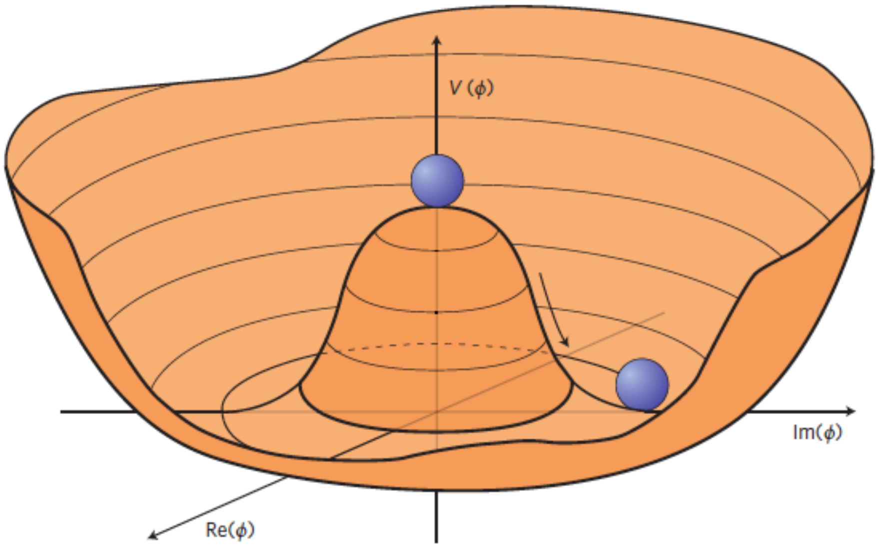

Figure 2.2: The Higgs potential energy $V(\phi)$, when $\mu^2 < 0$ [16].

with $\nu = 246$ GeV. This parameter is defined as the Electroweak scale. The scalar field develops a nonzero vacuum expectation value for $\mu^2 < 0$. This leads to a spontaneous breaking of the symmetry, specifically, it breaks the Electroweak Symmetry. That means $SU(2)_L \otimes U(1)_Y$ separate, which creates the $U(1)$ subgroup.

Seeing as the symmetry is broken, three massless gauge bosons ate three components out of the four components of the scalar Higgs field 2.21, the Goldstone bosons, to produce a physically massive vector field (a particle with mass). For additional information, see the Nambu-Goldstone theorem [21, 27].

As a result, three out of the four gauge bosons are massive (W^+, W^-, Z) and the photon (γ) remains massless. The charged bosons (W^+, W^-) are given by

$$W^{\pm} = (W^1 \mp iW^2)/\sqrt{2} \tag{2.27}$$

The neutral gauge bosons (Z, γ) are given as in equation 2.20

$$\begin{aligned} A_\mu &= B_\mu cos\theta_W + W_\mu^3 sin\theta_W \\ Z_\mu &= -B_\mu cos\theta_W + W_\mu^3 sin\theta_W \end{aligned} \tag{2.28}$$

where θ_W is the weak mixing angle or the Weinberg angle. The masses for these bosons are defined as

$$
\begin{aligned}
M_w &= \frac{g\nu}{2} = M_w = 80.385 \pm 0.016\,\text{GeV} \\
M_Z &= \frac{1}{2}\sqrt{g + g^{,}}\nu = M_z = 91.1876 \pm 0.0021\,\text{GeV} \\
M_\gamma &= 0
\end{aligned}
\tag{2.29}
$$

where g is the SU(2) gauge coupling and $g^{,}$ is the U(1) gauge coupling. The mass of the Higgs boson, which was measured at CERN in 2012 [ATLAS and CMS experiments], is given by

$$
M_H = \sqrt{2}\nu = 125.10 \pm 0.14\,\text{GeV} \tag{2.30}
$$

In summary, spontaneous symmetry breaking that triggers the Higgs mechanism breaks the $SU(2)_L \otimes U(1)_Y$ symmetry, which explains how gauge bosons and fermions (such as electrons) acquire masses. [27, 21, 12, 33, 25, 28, 18]

2.3 Beyond the SM physics model

The insufficiency of the Standard Model theory is thoroughly described in section 2.1. It sparked the development of new theories that go beyond the Standard Model in attempts to discover the Full Model. This section goes into detail about two resonance benchmark theories which will be discussed in this thesis. The first one is called the Heavy Vector Triplet HVT parametrization, which can predict a $W^{'}$ resonance produced by quark-antiquark Fusion (section 2.6.2) or Vector Boson Fusion VBF (section 2.6.1). The second benchmark is called the Georgi-Machacek Model, which can predict a charged Higgs scalar $H^{\pm}$ and is produced only in Vector Boson Fusion VBF.

2.3.1 Heavy Vector Triplet HVT

This section provides a brief overview of the Heavy Vector Triplet HVT. For a deeper understanding of HVT see [31, 18]. The Heavy Vector Triplet (HVT) is a simplified phenomenological Lagrangian approach where a simplified model strategy is used. But what exactly is a simplified model strategy and why is it indispensable? The extensions of the Standard Model theory tend to be more complex in data compared to the initial theory because there are hundreds of parameters that must be dealt with. To put it briefly, the idea of simplified model strategy is to restrict the parameters area. Reducing the number of parameters allows for easier calculation, therefore making it easier to detect and describe evidence of new physics. By way of illustration, the resonant searches are not sensitive to all kinematic variables and not to all free parameters of the studying model, but only to parameters which control the mass of the resonance, also the parameters related to the production and decay of resonance.

[6, 31].

A simplified phenomenological Lagrangian is used in the HVT model. It predicts three new vectors in high mass scale (TeV), $V_\mu^a, a = 1, 2, 3$, with spin-1 bosons. Two of them are charged and the third one is neutral. The charge eigenstate is given by the following:

$$V_\mu^\pm = \frac{V_\mu^1 \mp iV_\mu^2}{\sqrt{2}}, V_\mu^0 = V_\mu^3 \tag{2.31}$$

The simple phenomenological Lagrangian for new vectors, which includes the V kinetic and mass terms, SM interactions and HVT interactions, is given by the following equation as in [31] :

$$\begin{aligned}
\mathcal{L}_V = &-\frac{1}{4}D_{[\mu}V_{\nu]}^a D^{[\mu}V^{\nu]^a} + \frac{m_V^2}{2}V_\mu^a V^{\mu a} \\
&+ ig_V c_H V_\mu^a H^\dagger \tau^a \overleftrightarrow{D}^\mu H + \frac{g^2}{g_v} c_F V_\mu^a J_F^{\mu a} \\
&+ \frac{g_v}{2} c_{VVV} \epsilon_{abc} V_\mu^a V_\mu^b D^{[\mu}V^{\nu]^c} + g_V^2 c_{VVHH} V_\mu^a V^{\mu a} H^\dagger H - \frac{g}{2} c_{VVW} \epsilon_{abc} W^{\mu\nu a} V_\mu^b V_\nu^c
\end{aligned} \tag{2.32}$$

The term $(iH^\dagger \tau^a \overleftrightarrow{D}^\mu H)$ describes the interaction between V and Higgs current. $J_F^{\mu a}$ is the SM left-handed fermionic current and g refers to $SU(2)_L$ gauge coupling. It is crucial to refer to the parameters c_H and c_F. The V interaction with the SM vectors and with the Higgs field is controlled by c_H. c_H is also responsible for Vector Boson Fusion VBF production and the decay of the vector boson. The parameter c_F is responsible for the Drell-Yan production [20] and the decay into fermions in this production. c_F describes the direct couplings to fermions. There are two coupling constants (g_V, g) in lines two and three, where the strength of V is represented by g_V. The equation 2.32 is fully described in [31].

The HVT particles can be produced in quark-fusion and Vector Boson Fusion (VBF), which are the production modes that are studied in this thesis. Therefore, it is important to have HVT as a benchmark model.

Finally, there are two explicit models in HVT (as in ref [31]), Model A and Model B. Model A is an extended gauge symmetry (here g_V=1) and Model B is a minimal composite Higgs model (here g_V=3),[31, 18].

2.3.2 Georgi-Machacek GM

The second example of a theory going beyond the Standard Model, which will be referred to as benchmark in this thesis, is an extension of the Standard Model in the Higgs sector called the Georgi-Machacek Model. The GM Model is custodial-symmetric $SU(2)$. It preserves the electroweak parameter ρ at tree level, as described by the following equation:

$$\rho = \frac{M_W^2}{M_Z^2 \cos^2 \theta_W} = 1 \tag{2.33}$$

The GM Model contains three different fields with different values of Y, where Y is the hypercharge, defined in equation 2.4. These fields are:

- an isospin doublet filed ϕ, with $Y = \frac{1}{2}$
- a complex triplet field χ, with $Y = 1$
- a real triplet field ξ, with $Y = 0$

To specify, the SM Higgs sector is extended by one complex triplet field χ and one real triplet field ξ.
The custodial SU(2) symmetry can be observed when the fields are expressed in the following form:

$$\Phi = \begin{pmatrix} \phi^{0*} & \phi^+ \\ -\phi^- & \phi^0 \end{pmatrix}, \quad \Delta = \begin{pmatrix} \chi^{0*} & \xi^+ & \chi{++} \\ -\chi^- & \xi^0 & \chi{+} \\ \chi^{--} & -\xi^- & \chi 0 \end{pmatrix} \tag{2.34}$$

where the bidoublet Φ and the bitriplet Δ are transformed under $SU(2)_L \otimes SU(2)_R$ as:

$$\begin{aligned} &\Phi \to U_L \Phi U_R^\dagger \quad and \quad \Delta \to U_L \Delta U_R^\dagger \\ &with \quad U_{L,R} = exp(i\theta^a_{L,R} T^a) \end{aligned} \tag{2.35}$$

The neutral components ϕ^0, χ^0 and ξ^0 in equation 2.34 can be written as:

$$\phi^0 = \tfrac{1}{\sqrt{2}}(\phi_r + \nu_\phi + i\phi_i), \quad \chi^0 = \tfrac{1}{\sqrt{2}}(\chi_r + i\chi_i) + \nu_\chi, \quad \xi^0 = \xi_r + \nu_\xi \tag{2.36}$$

The ν_ϕ, ν_χ and ν_ξ in equation 2.36 represent the vacuum expectation values of ϕ, χ and ξ fields. As mentioned earlier, the GM Model is custodial symmetric $SU(2)$. The symmetry exists assuming that $\nu_\chi = \nu_\xi \equiv \nu_\Delta$, which means $SU(2)_L \otimes SU(2)_R \to SU(2)$.
Depending on the observed mass of W and Z gauge bosons, the vacuum expectation values are supposed to have the following value:

$$\nu^2 = \nu_\phi^2 + 8\nu_\Delta^2 = \frac{1}{\sqrt{2}G_F} \simeq (246\, GeV)^2 \tag{2.37}$$

Consequently, the physical mass spectrum can be categorized into three states:

- 2 singlet state (h, H)
- a fiveplet (5-plet)

- a triplet (3-plet)

As in section (COLLIDER PHENOMENOLOGY) in [14], the 5-plet H_5 can couple to gauge boson pairs, similarly to the Vector Boson Fusion VBF process. This justifies having the 5-plet as a benchmark in this thesis. For more physical and mathematical details, see [14, 19, 9].

2.4 Resonance searches

This thesis focuses on the search for resonant di-boson VV production, where ($V = W^{\pm}$, Z $\rightarrow \ell\ \nu\ \ell\ell$). It is a direct search for "bumps" in the invariant mass spectra that represent new particles. Resonance is one of the simplest methods of looking for physics beyond the Standard Model (BSM) and discovering new particles. A resonant excess is a statistically significant bump on top of the smooth Standard Model background.

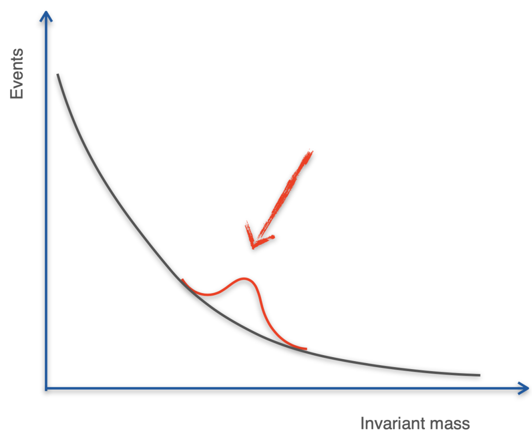

Figure 2.3: Illustration of a bump on top of a smooth background.

Mass reconstruction and resolution are crucial in resonance searches, considering the fact that the statistical power is inversely proportional to the mass resolution and the resonance could be hidden by bad understanding of resolution.
In the fully leptonic channel, the electrons and muons are fully reconstructed, but the neutrino momenta is missing. The W boson mass constraints will be used to recover the invariant mass of the system.
As the Z boson decays into two leptons (electrons or muons) of the same flavor and opposite charge, these leptons can be easily detected in the detector. The following equation will be used to reconstruct the invariant mass of the Z boson:

$$M_Z^2 = m_1^2 + m_2^2 + 2(E_1E_2 - p_1p_2\cos\theta) \tag{2.38}$$

where m_1, m_2, E_1, E_2 and p_1, p_2 are the masses, energies and momentums of outcoming leptons, and θ is the polar angle between the positive direction of beam axis and the particle

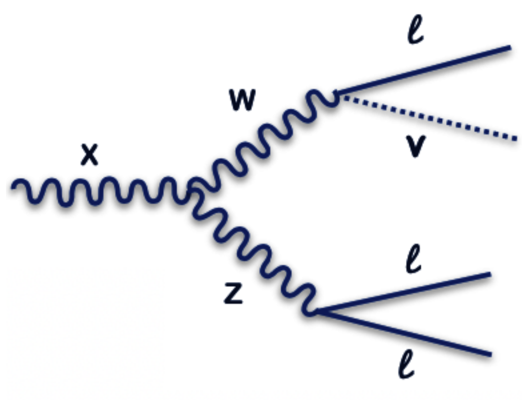

Figure 2.4: Feynman graph for the WZ decay mode into leptonic channel

three momentum. The W boson decays into a lepton (electron or muon) and its corresponding neutrino. In this case, the equation 2.38 cannot be used because the neutrinos escape from the detector without being detected. The energy and the momentum of the neutrino is missing, although it is expected to cause the energy and momentum conservation in the transverse plane. This leads to the following equation:

$$M_W^2 = m_1^2 + m_2^2 + (2E_{T1}E_{T2} - p_{T1}p_{T2}\cos\theta) \tag{2.39}$$

M_W is the transverse mass of the W boson, E_T is the transverse energy, and p_T is the transverse momentum. For massless particles such as neutrinos $m_2 = 0$.

2.5 WZ decay modes and selection criteria

2.5.1 W and Z bosons

As mentioned in the previous sections, the $W^{\pm}$ and Z bosons are the carriers of the weak force. This section describes their production and decay modes, as they are the vector bosons that are studied in this thesis.

$W^{\pm}$ bosons

On 25 January 1983, CERN announced the discovery of the W boson to the scientific community. The W boson is an elementary particle which is responsible for carrying the weak force. It is an electrically charged boson that can havd either positive or negative charge. Scientists at the US laboratory Fermilab have provided precise measurements for the W boson mass: $M_w = 80.385 \pm 0.016\ GeV/c^2$ [3] , $Spin = 1$. W bosons are massive and due to this fact they have a short lifetime (half-life of about 3×10^{-25} s). Therefore W bosons decay into pairs of fermions, either into a lepton and an anti-neutrino, or into a quark and an anti-quark (except the top quark).

Z boson
The Z boson was also discovered in 1983 by scientists at CERN. It is the second boson, which is responsible for carrying the weak force together with the $W^{\pm}$ boson. In contrast to the $W^{\pm}$ bosons, the Z boson has no electric charge. Its mass, M_Z, equals 91.1876 ± 0.0021 GeV/c^2 and its $Spin = 1$. However, similar to the $W^{\pm}$ bosons, it also decays to a fermion and its antiparticle.

2.5.2 WZ decay modes

Before describing WZ decay modes, it is important to state that spending time and efforts on studying the properties of $W^{\pm}$ and Z bosons and their interactions is essential for gaining a deep understanding of the electroweak symmetry breaking (EWSB) and the key to discovering physics beyond the Standard model (BSM).
Overall, there are three different kinds of diboson (scattering) channels associated with W and Z production: WW, WZ and ZZ. In this thesis, only WZ production will be considered. In figure 2.5 the measurements of several Standard Model cross sections in ATLAS at $\sqrt{s}$= 7,8 and 13 TeV are plotted, compared to the corresponding theoretical expectations [5]. It can obviously be seen that the cross-section of WZ production is higher than the production of ZZ production. WW production definitely has the highest cross section channel among all diboson channels, however, working with this channel is challenging to deal with and hard to distinguish between its events and $t\bar{t}$ events. There are also two neutrinos in the final state, which makes the reconstruction of the kinematics of events significantly more challenging. For more details see [13].
As mentioned before, the WZ production can decay into two pairs of fermions. All possible decay channels can clearly be seen in pie chart design 2.6. Without doubt, fully hadronic decays have the largest branching fractions but they also contain more background from QCD and multijet events. Because of that, another decay mode is going to be considered instead. In this thesis, the measurements are performed in the fully leptonic decay modes WZ $\rightarrow l\ \nu\ l\ l$ where l= e or μ, despite the fact that it has just 1.6 % branching fractions of the total number. The fully leptonic decay modes have certain advantages such as their clean signature and small background, which encourages many researches to focus on them.

2.5.3 WZ diboson selection

The present analysis describes a search for resonant structure in WZ production using data collected by the ATLAS detector. Only the fully leptonic final state WZ $\rightarrow l\ \nu\ l\ l$ is going to be considered, where l= e or μ, with luminosity L =138.7 $fb^{-}1$ at center of mass $\sqrt{s}$ = 13 TeV (according to data from LHC full Run-2 (2015-2018)). These are all possible final states

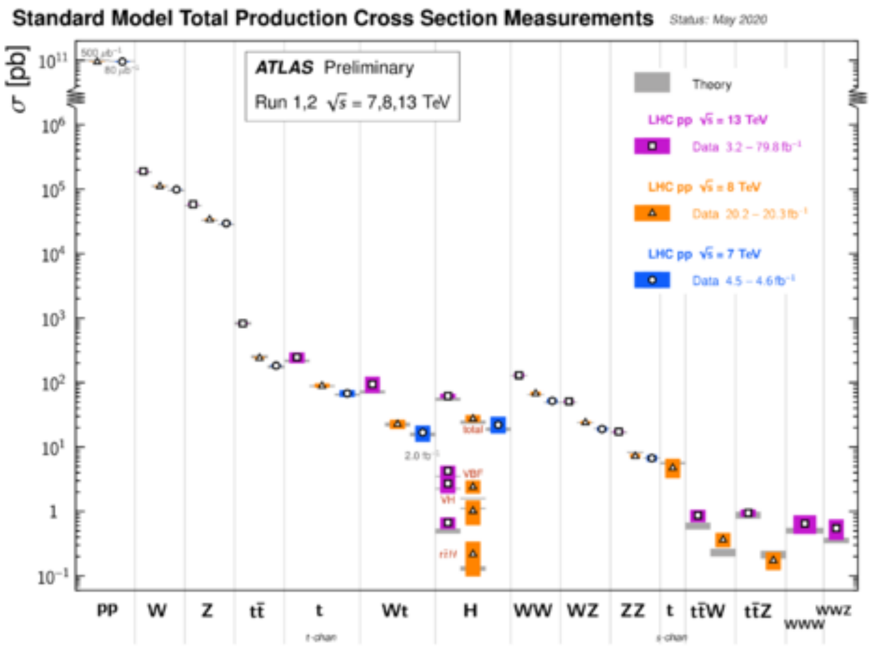

Figure 2.5: Summary of different cross section measurements for different Standard Model productions, also the theoretical expectations are shown for Run 1 and 2. From [5]

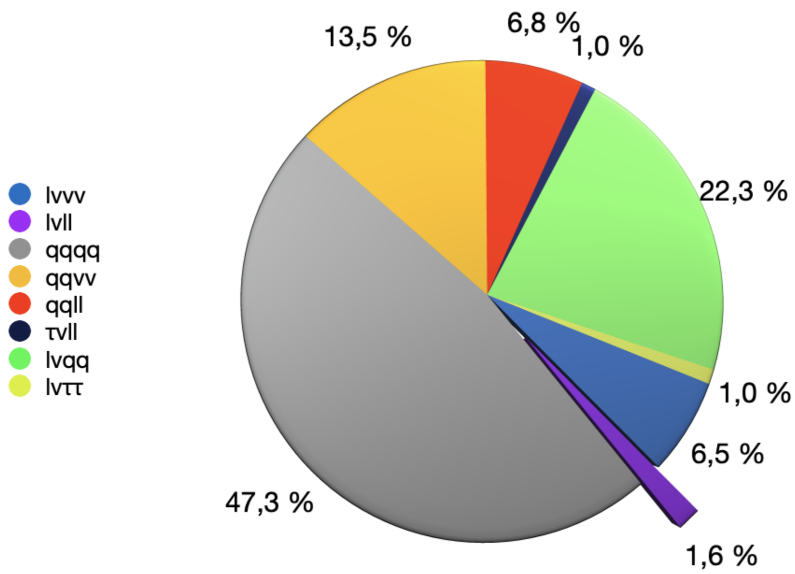

Figure 2.6: A pie chart describes the WZ decay modes for different channels in percentage.

with e and μ:

- μ^- μ^+ $\mu^\pm$ ν
- μ^- μ^+ $e^\pm$ ν
- e^- e^+ $\mu^\pm$ ν
- e^- e^+ $e^\pm$ ν

Lepton selection

Seeing as all channels are leptonic, leptons are essential, therefore it is important to apply precise cuts and conditions after lepton reconstruction to ensure that the required leptons are featured in the total event yield (for more information about reconstruction algorithms see[12]). One of the parts of the ATLAS detector is the Trigger level, where the dimuon and the dielectron are recorded using different trigger levels. Any high p_T leptons ($p_T > 15$ GeV) that originate from the primary vertex will pass the selection criteria. As a result, 3 high efficiency leptons are obtained and the background is reduced from jet, Z+jet, QCD, tt and single Top.

Z boson selection

The events must have at least two isolated leptons of same flavour and opposite charge. In a case where the event has more than one pair of leptons, the selection must be performed in the event where the invariant mass ($m_{\ell\ell}$) is closest to the Z mass. Applying the Z selections will reduce non-peaking backgrounds such as tt, single Top and WW+jets.

W boson selection

Since the W boson decays into a lepton and its anti-neutrino, the W mass can not be fully reconstructed like Z mass. Therefore, the third lepton, which is associated with the W boson, must have a high pt > 20 GeV and the missing transverse Energy, which makes calculation of the neutrino mass possible, should be > 25 GeV. As a result, the backgrounds are reduced from the Z+jets and top. In further sections the backgrounds of the single regions are going to be described in more detail.

2.6 Production Modes

Many theories that lie beyond the Standard Model predict the vector and scalar resonances production modes. These resources could be produced by several production modes. The events in thesis are studied in the following production modes:

- Vector Boson Fusion VBF
- quark/gluon Fusion

After imposing selection criteria of the WZ bosons on the events, the candidate events are separated into two different types of production modes: $q\bar{q}$ and VBF.

2.6.1 VBF production mode

The VBF production mode contains specific events with two energetic forward jets with high dijet invariant mass of at least 500 GeV, separation in rapidity $\Delta\eta > 3.5$ and $\eta < 2.5$, and the 3 specific leptons with $p^T > 25$ GeV and ($|\eta| < 2.5$). The leading lepton $p^T > 27$ GeV. Figure 2.7 shows a Feynman diagram of the VBF production modes.

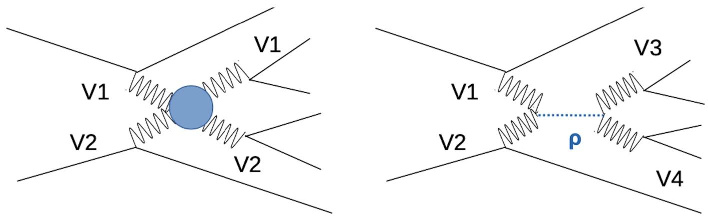

Figure 2.7: A Feynman diagram of the VBF production modes

2.6.2 qq production mode

The second production mode category is $q\bar{q}$, which includes all other events. Both the 3 specific leptons with $p^T > 25$ GeV and ($|\eta| < 2.5$) and (p_z^T/mWZ > 0.35 and p_w^T /mWZ > 0.35) cuts are applied in this region. Figure 2.8 shows a Feynman diagram of the $q\bar{q}$ production mode.

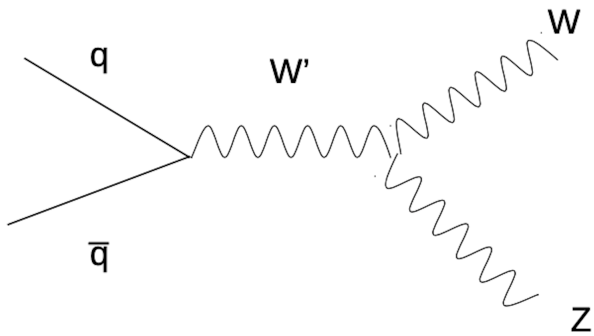

Figure 2.8: A Feynman diagram of the $q\bar{q}$ production mode

3 Experiment

As a theory the Standard Model is incomplete and does not answer many questions such as: What are dark matter and dark energy? Is there any evidence for the existence of supersymmetry? and many more. The main purpose of building a machine like the LHC is to provide answers for these questions. The data in this thesis was collected at ATLAS in 2015-2018 during full Run 2 of the Large Hadron Collider.

3.1 LHC

In order to study the behaviour of particles they need to be produced first. Currently the most successful and practical way of doing it is through the use of an accelerator. Particles are accelerated to a particular speed, after which they are collided with one another or into a fixed target. Depending on the required amount of energy and on the purposes of the experiment, the accelerators are built in three different designs:

- linear accelerator
- synchrotron accelerator
- cyclotron accelerator

The data for this thesis was collected from the ATLAS (A Toroidal LHC ApparatuS) detector at the LHC (the Large Hadron Collider) at CERN (the European Organization for Nuclear Research) in Switzerland. The LHC is the highest-energy synchrotron particle accelerator, the largest scientific device ever built. In this huge collider protons are accelerated around a 27 km long ring to a speed that is close to the speed of light, after which they are collided inside the particle detectors: CMS, LHCb, ATLAS, and ALICE, which can be seen in figure 3.1. The 27 kilometres long tube is packed with 9593 magnets. Some magnets are used to accelerate protons and keep them moving straight on their track as they head down the tube. Others help impart a slight curve so that the protons go around the circular path of the LHC. The LHC contains two beam pipes going in opposite directions. The beams are made up of bunches of protons. One beam has 1404 bunches. Each bunch has about 100 billion protons. Using superconducting magnets operating at a temperature of 1.9 K, it is possible to keep the beams flying with a velocity near the speed of light (99.9999991% the speed of light). After

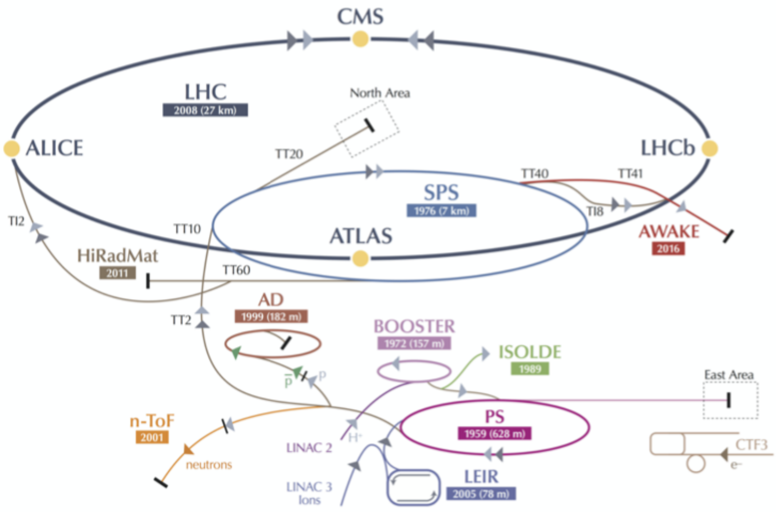

Figure 3.1: Illustrative design of the LHC with four detectors: CMS, LHCb, ATLAS, and ALICE.[22]

achieving an energy of 6.5 TeV for each beam, they can be collided at the four main detectors (mentioned above) at 13 TeV. For more details, see reference [17].

3.2 ATLAS

The LHC has four interaction points. Each of these points is covered by a detector. The ATLAS detector is the largest volume detector ever constructed for a particle collider. The general ATLAS detector design is shown in figure 3.2. It is massive: 25 meters in height, 44 meters in length, weighing approximately 7000 tonnes. Additionally, it has around 100 million electronic channels and 3000 km of cables. This enormous machine has been built for a number of purposes such as: the investigation of the Standard Model properties, the search for the Higgs boson, extra dimensions, and any evidence for the existence of dark matter as well as dark energy. For more details about the structure, development, and operation of the ATLAS detector, see references[8][32].

3.2.1 ATLAS coordinate system

Every detector in LHC has specific properties and features so as to cover a wide range of possible results. The ATLAS detector employs a right-handed Cartesian system with the x-axis pointing towards the centre of the LHC accelerator ring and the y-axis pointing upwards. The z-axis is parallel and anti-parallel to the LHC beam axis. As is known, the ATLAS has a cylindrical shape, therefore it is convenient to describe it using a cylindrical coordinate system (r,ϕ), where ϕ is the azimuth angle measured from the x-axis, around the beam axis.

The ATLAS detector design is symmetrical in ϕ. The rapidity Y is defined through the use of 4-momentum as in equation 3.1 for massive particles.

$$Y = \frac{1}{2} \ln \frac{E + p_z}{E - p_z} \tag{3.1}$$

The pseudorapidity η, defined in equation 3.2, describes the angle of a particle relative to the beam axis (z-axis), where θ is the polar angle, defined as the angle from the positive z-axis. Fortunately, for massless particles η and Y are the same. The coordinate system with the angles θ and ϕ for ATLAS is illustrated in Figure 3.3

$$\eta = -\ln \tan(\frac{\theta}{2}) \tag{3.2}$$

In contrast to Y, η is invariant under Lorentz-boosts along the collision beam axis. The important angle separation ΔR in the η-ϕ space, defined in equation 3.3, is also invariant under Lorentz-boosts along the collision beam axis.

$$\Delta R = \sqrt{(\Delta\eta)^2 + (\Delta\phi)^2} \tag{3.3}$$

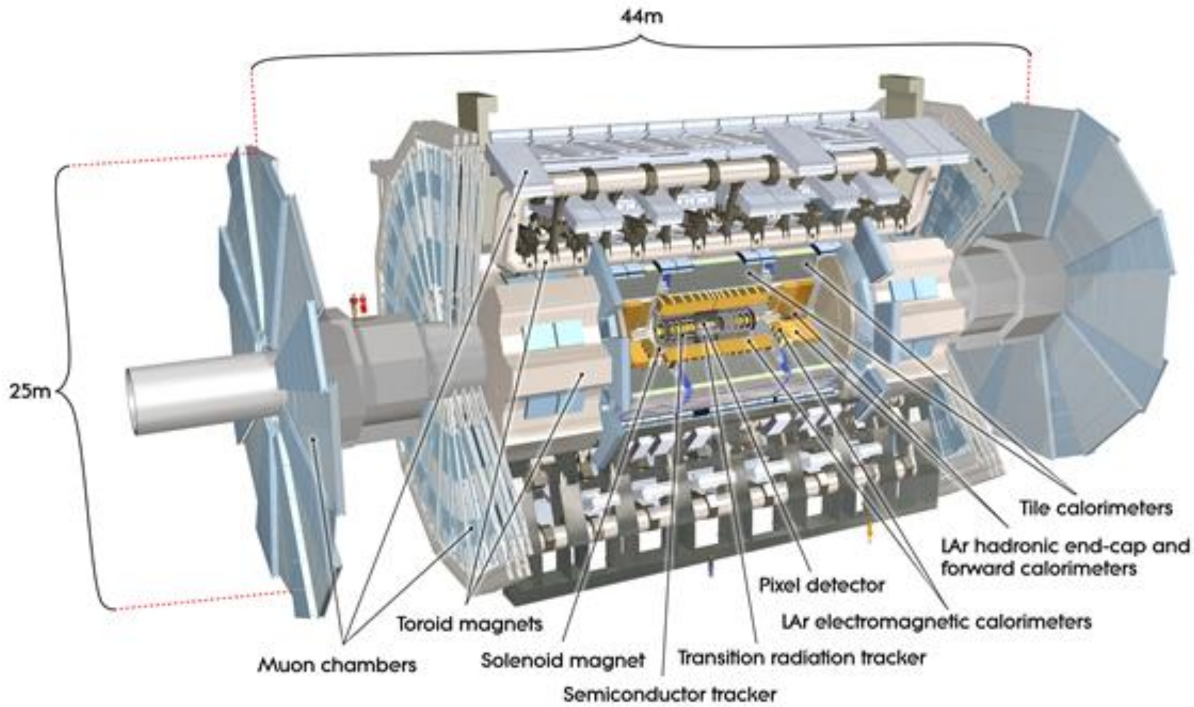

Figure 3.2: A schematic layout of the ATLAS detector [8].

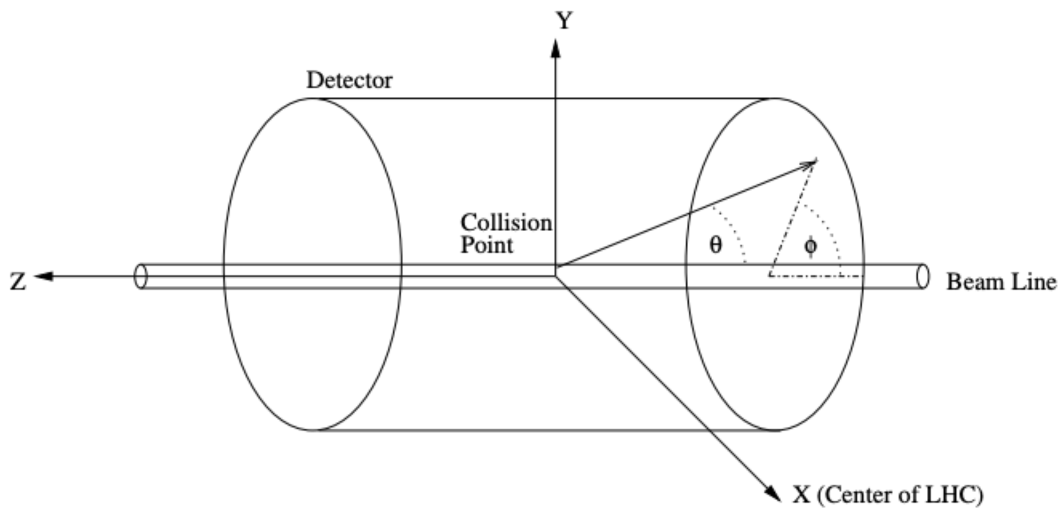

Figure 3.3: The coordinate system used by the ATLAS detector [32].

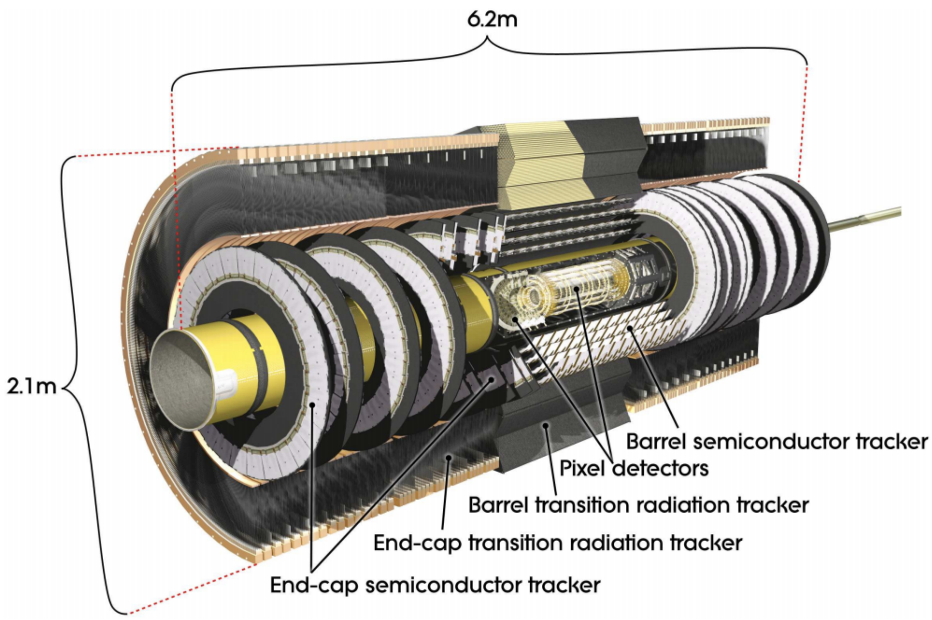

Figure 3.4: Cut-away view of the ATLAS inner detector (ID) [8].

3.2.2 The Inner Detector

At a beam luminosity of $10^{34}\ cm^{-2}\ s^{-1}$, there will be about 20 collisions per bunch crossing, around 40 million bunch crossings per second, approximately 1 billion collisions per second. The particles emerging after collisions create a very high density. To measure the momentum and vertex resolution in high-precision for collisions like these, ATLAS is intended to record the tracks and energy of the particles appearing as a result of these collisions. ATLAS has seven different detecting sub-systems arranged in layers around the collision point to capture any evidence of particles that have been produced in the collisions. Each sub-system is sensitive to different types of particles. Closest to the interaction point is the ATLAS inner detector (ID). The layout of the ID is illustrated in figure 3.4. The ID is 6.2 meters in length and 2.1 meters in height. It operates in a 2 Tesla magnetic field. The ID is used to measure the momentum of each charged particle as they traverse (cross) the detector. As charged particles, they deposit a small amount of energy on their tracks, which allows us to reconstruct the particles' trajectory. Charged particles with transverse momentum above 500 MeV can be reconstructed in the ATLAS ID. The information obtained from the ID detector is used to reconstruct particles such as electrons and muons.

The ID consists of three sub-detectors: Pixel detector, Semiconductor Tracker (SCT), and Transition Radiation Tracker (TRT). Figure 3.5 depicts a cut-away of the ID barrel. Figure 3.6 illustrates a cut-away of one of the ID end-caps.

In addition to that, the tracking detectors (pixel and SCT) provide important information about the vertex, which can be used later to reconstruct and identify the particles and their lifetime. The pixel detector and SCT detector cover the region η <2.5. The pixel detector is

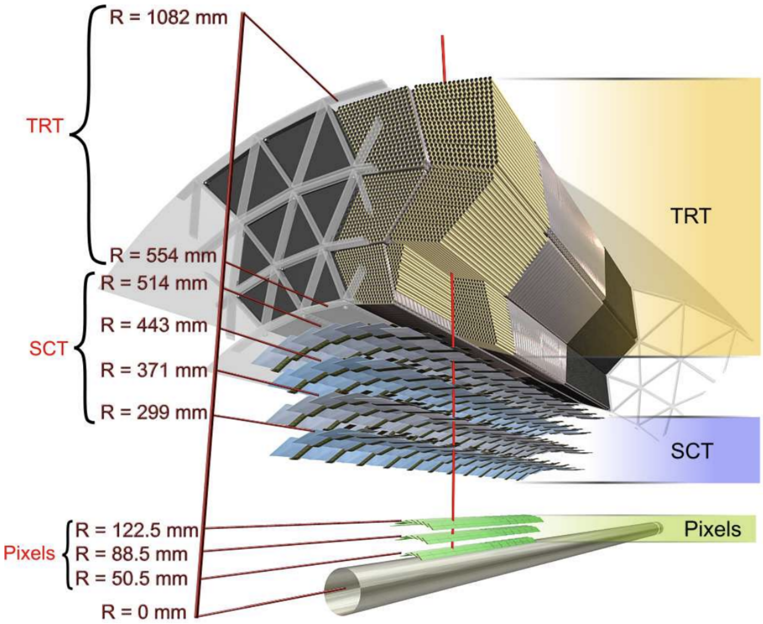

Figure 3.5: Illustration of the ATLAS inner detector demonstrating pixels, SCT, and TRT [8].

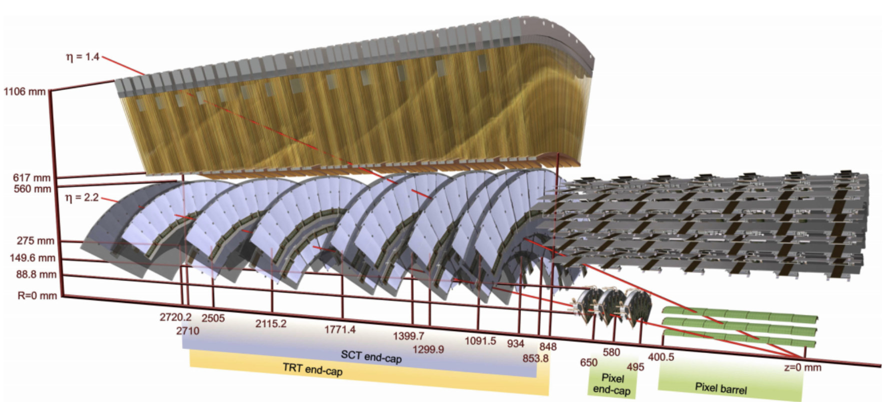

Figure 3.6: A cut-away of one of the ID end-caps [8].

in closest proximity to the collisions, it contains 80 million pixels (80 million channels), each pixel has a size 50 $\times$ 400 μm. The pixel detector has an accuracy of 10μm in the $r-\theta$ plane and 115 μm in z-axis. The SCT detector surrounds the pixel detector, which is comprised of narrow silicone strips in the size 80 μm $\times$ 12 cm. A silicon microstrip tracker consists of 4088 two-sided modules and over 6 million implanted readout strips (6 million channels). The SCT detector has an accuracy of 17μm in the $r-\theta$ plane and 580 μm in z-axis. The TRT (Transition Radiation Tracker) surrounds the pixel and SCT detectors. It is the largest part of the ID, with the volume 12 m^3 and 350 000 read-out channels. The TRT detector has an accuracy of 130μm in the $r-\theta$ plane. All this information and more about the ID, pixel, SCT, and TRT can be found in references [8] [4].

3.2.3 The Calorimeter System

P-P collisions at high energy (∼13 TeV) produce a number of various types of particles such as hadrons (particles that contain quarks, such as neutrons and protons), muons, neutrinos, electrons, photons, etc. It is crucial to accurately measure the energy and momentum of these produced particles in order to be able to properly capture and identify them. ATLAS has calorimeters that measure the energy a particle loses as it passes through the detector. Usually the calorimeters are built to capture most of the particles emerging from the collision, except for muons and neutrinos. Figure 3.7 is an overview of the ATLAS calorimeter system, with the coverage $\eta < 4.9$. ATLAS has several types of calorimeters, which are arranged as barrels placed in both the centre and the end of the detector. The layers of calorimeters are made of steel, lead, and a special material which lights up when the particles pass through. Calorimeters consist of layers of a thick "absorber" material (such as, for example, copper) that fully absorbs incident particles and layers of an active material (e. g. Liquid argon) that produces an output signal proportional to the input energy. The calorimetry system of ATLAS includes the Liquid Argon (LAr) Calorimeter and the Tile Hadronic Calorimeter. The LAr calorimeter works with Liquid Argon at $-183\,^{\circ}$C. The LAr endcap consists of the forward calorimeter, electromagnetic (EM) and hadronic endcaps. The ATLAS EM endcaps are used to precisely identify electrons and photons and measure their energy as they interact with materials. The ATLAS Hadronic calorimeters, in turn, measure the energy deposition of hadrons. For more details see references[8] [4].

3.2.4 The Muon Spectrometer

The ATLAS detector is designed to identify and measure as many particles as possible. Due to a remarkably high mass of muons (105.7 MeV/c^2) as compared with electrons (0.511 MeV/c^2) or photons, muons cannot be stopped or measured in EM calorimeter or hadronic calorimeter. For this reason, the ATLAS has an additional special system called the muon spectrometer

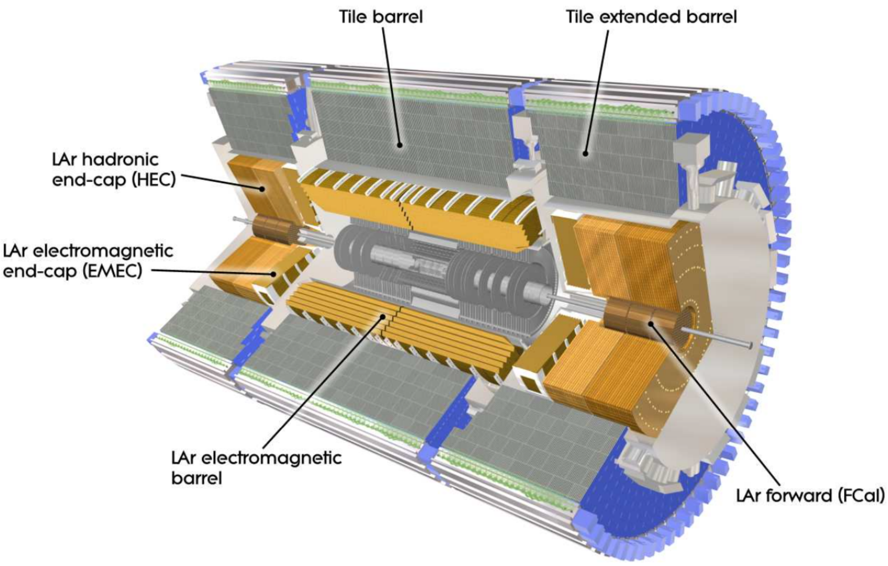

Figure 3.7: The calorimeter system of the ATLAS detector [8].

(MS) that is used for precisely measuring the position and the energy of muons. The information obtained from the MS, ID and calorimeter sub-detectors is used in ATLAS algorithms to reconstruct the muons.

The design of the MS is shown in figure 3.8. The muon system consists of Thin Gap Chambers, Resistive Plate Chambers, Monitored Drift Tubes, and Cathode Strip Chambers. The MS operates in a toroidal magnetic field with an average field strength of 0.5 T, where muons are deflected with an energy above 6 GeV. It covers η <2.7. For more specific details see references [8] [4].

3.2.5 Magnet System

The particles passing through the detector are deflected by the magnetic field. The ATLAS magnet system consists of Central Solenoid Magnet, Barrel Toroid, and End-cap Toroids, which used to bend charged particles for momentum measurement as they pass through and out of the detector. See figure 3.9.

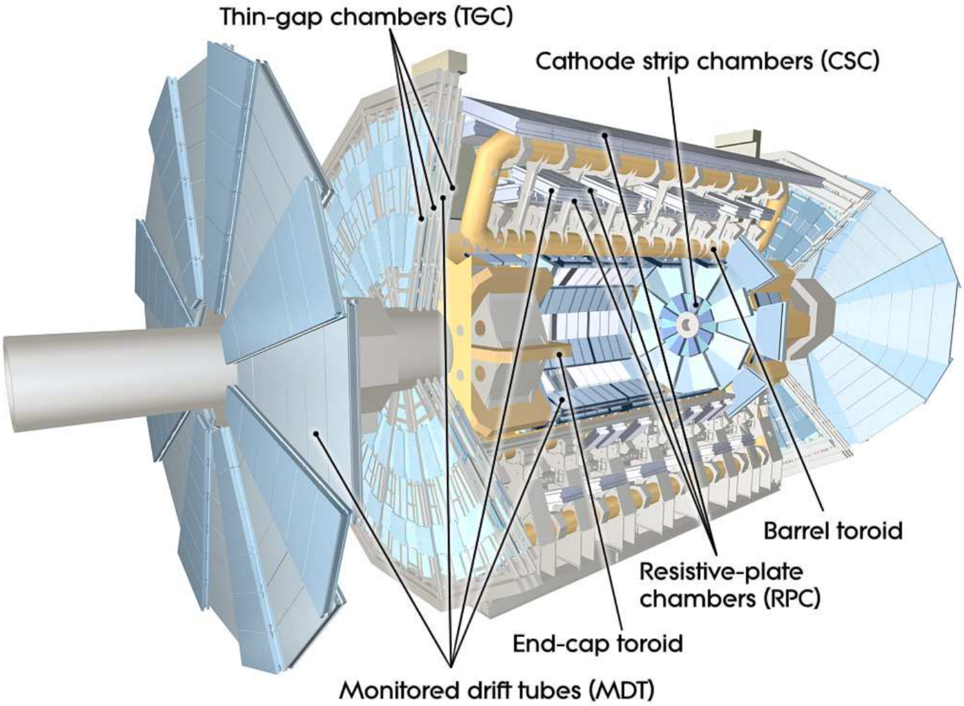

Figure 3.8: The muon spectrometer of the ATLAS detector [8].

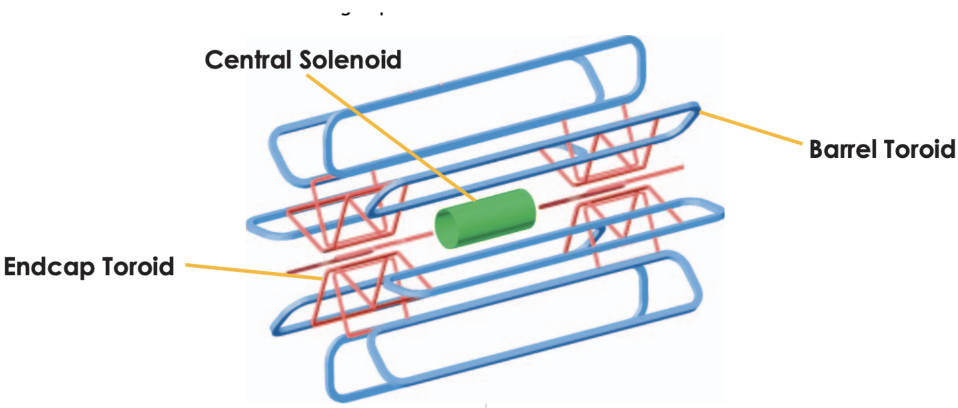

Figure 3.9: 3D view of the ATLAS magnet system [30].

3.3 Detector Objects

This section provides a brief overview of the identification and the reconstruction of the physics objects that are used in this thesis. The final state of the WZ $\rightarrow \ell\ \nu\ \ell\ell$ is three leptons and one neutrino ($\ell = e$ or μ). Therefore, the objects that are included electrons, muons and missing transverse energy.

Electron

The electrons are a type of particle that are produced in p-p collisions. The collision point is surrounded by various layers of the ATLAS sub-detectors. Electrons travel through the inner detector and lose their energy in the electromagnetic calorimeter, see figure 3.10. Electrons leave clear signatures in these ATLAS sub-detectors. Three different algorithms are used in the ATLAS detector for the reconstruction of electrons. Three different levels of identification of electrons are labeled loose, medium and tight. Every type of electron has been defined by specific variables. Electron reconstruction algorithms and required criteria for electron identification are described in detail in [24].

Muon

Unlike the electrons which are stopped in the electromagnetic calorimeter, muons can penetrate all layers of the ATLAS detector. Therefore the ATLAS detector has a special system called the muon spectrometer which is built in the outermost layer of the ATLAS detector. The muon spectrometer can provide precise measurements of the position and the energy of muons that travel through it. There are four types of muon reconstructions defined in ATLAS analysis: Stand-alone reconstruction, Combined reconstruction, Segment Tagged and Calorimeter Tagged Muons [24].

Missing transverse energy

The ATLAS detector was built with different layers of sub-detectors and high measuring efficiency to be capable of detecting all possible outcome particles and their properties (e.g. mass, momentum, direction, etc.) that are produced in the p-p collisions. In spite of this, there are particles that escape the ATLAS detector without being detected. These particles (in this thesis, neutrinos) are expected to cause the energy and momentum conservation in the transverse plane. The following equation defines the missing transverse energy:

$$E_T^{miss} = \sqrt{(E_x^{miss})^2 + (E_y^{miss})^2} \tag{3.4}$$

The ATLAS system provides different tools fot reconstruction of the missing transverse energy E_T^{miss}. In this thesis, the METMakerTool is used to reconstruct the E_T^{miss}.

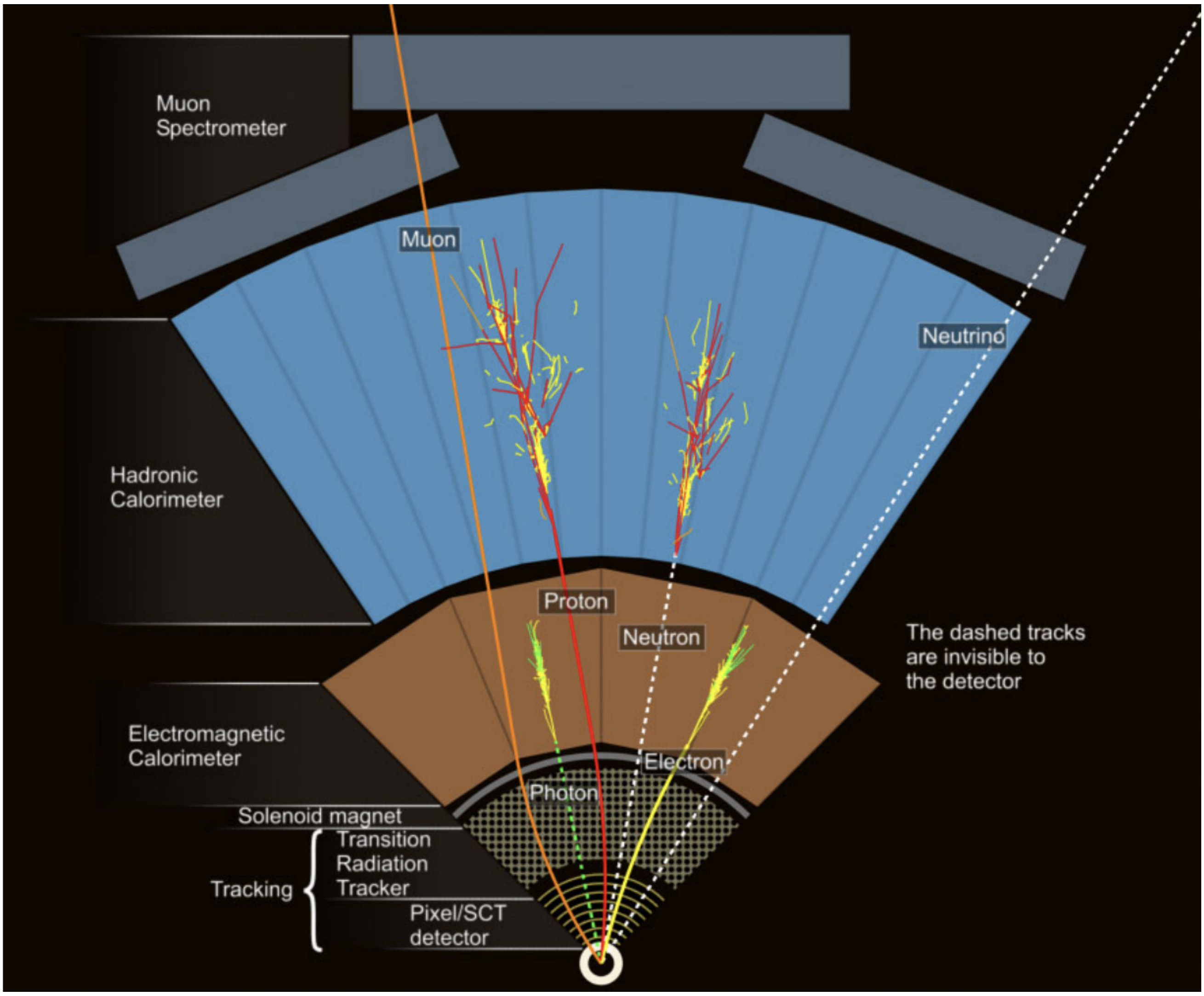

Figure 3.10: View of the ATLAS sub-detectors [26].

4 Study on the selected Events

4.1 Event selection

The present analysis describes the search for resonance structure in WZ production using data collected by the ATLAS detector. Only the leptonic final states will be considered WZ $\rightarrow \ell$ ν $\ell\ell$ ($\ell = e$ or μ) in full Run 2 (2015-2018), with luminosity $L = 138.7 fb^{-1}$ at $\sqrt{s} = 13$ TeV. Since the fully leptonic decay of the $W^{\pm}Z$ boson pairs is considered, these are all final states with electrons and muons for $W^{\pm}Z$ events:

- μ^- μ^+ $\mu^{\pm}$
- μ^- μ^+ $e^{\pm}$
- e^- e^+ $\mu^{\pm}$
- e^- e^+ $e^{\pm}$

The event selection criteria start with the definition of an inclusive $W^{\pm}Z$ phase space, which involves a number steps of events selection. These steps are listed in table 4.1

Inclusive event selection	
Event cleaning	Reject LAr, Tile and SCT corrupted events and incomplete events
Primary vertex	Hard scattering vertex with at least two tracks
Trigger	Single lepton trigger
Jet cleaning	pass DFCommonJetseventCleanLooseBad
ZZ veto	Less than 4 “soft” leptons
N leptons	Exactly three leptons passing the “loose ” lepton selection
Z candidate	built from Same-Flavor-Opposite-Sign (SFOS)lepton pair with M_{ll} closest to Z PDG mass
W candidate	built from the third lepton and E_T^{miss}
W, Z selection	Z leptons passing “tight(Z)" lepton selection W leptons passing “tight(W)" lepton selection
Mass window	$\|M_{ll} - M_Z\| < 20$ GeV
Missing Energy	$E_T^{miss} > 25$ GeV
Leading lepton p_T	Leading Lepton $p_T > 27$ Gev

Table 4.1: The table of event selection criteria for inclusive region [2].

From this region, two signal regions will be defined with specific additional criteria for each one of them: the VBF cut-based signal region and the $q\bar{q}$ signal region. These two single regions will be described in the following section.

4.1.1 Definitions of VBF cut-based and qq signal regions

In the VBF signal region, the events must pass the inclusive $W^{\pm}Z$ selection. Aside from that, the VBF category applies more additional cuts. It contains events with two energetic forward jets with high dijet invariant mass at least 500 GeV, separation in rapidity $\Delta\eta > 3.5$ and $\eta <$ 2.5. These are also 3 leptons with $p^T > 25$ GeV.
If the events fail the VBF cut-based selection, they will be considered in qq selection. There are two additional cuts applied in this region: precisely 3 leptons with $p^T > 25$ GeV and ($|\eta|$ < 2.5) and (p_z^T/mWZ > 0.35 and p_w^T /mWZ > 0.35) cuts are applied in this region.

4.2 Invariant mass in the VBF and qq signal regions

In figure 4.1a and 4.1b depicts the distribution of the $W^{\pm}Z$ invariant mass in $q\bar{q}$ and VBF signal regions, which will be used for limiting the extraction. It has a smooth falling shape after 300 GeV, in figure 4.1b (one MC event with a high weight). This thesis focuses on the description of the main background. The main background in both signal regions is the SM WZ production. As the numbers show in table 4.2a and 4.2b , the WZ production represents $\simeq$ 89% from the total number of events in qq signal region and $\simeq$ 91% in the VBF single region. The total background contributions come from WZ, ZZ, tZ, W/Z+jets, W/Z+gamma, ttV and VVV. The background itself separates into two categories:

- irreducible background (WZ, ZZ, tZ and ttV)
- reducible background (W/Z+jets, W/Z+gamma and VVV)

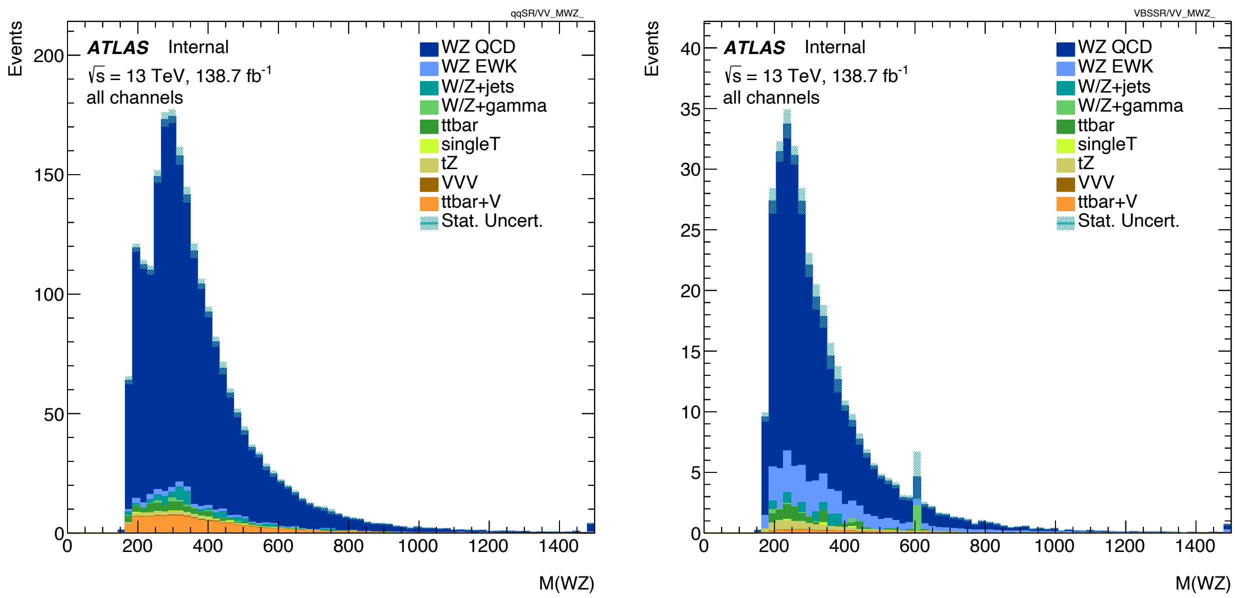

(a) $q\bar{q}$ Signal Region (b) VBF Signal Region

Figure 4.1: Obseved distributions of the WZ invariant mass in $q\bar{q}$ and VBF signal regions.

		+/-
WZ QCD	1865	8
WZ EWK	34,9	0,2
W/Z+jets	39	6
W/Z+gamma	7	1
ttbar	40	3
singleT	3,8	0,8
tZ	22	0,1
VVV	7,3	0,1
ttbar+V	114	0,8
total BKG	2133	11

(a) $q\bar{q}$ signal region

		+/-
WZ QCD	257	2
WZ EWK	44,8	0,2
W/Z+jets	6	2
W/Z+gamm	3	2
ttbar	8	1
singleT	0,5	0,3
tZ	8,1	0,1
VVV	0,8	0,04
ttbar+V	3,03	0,04
total BKG	332	0,13

(b) VBF signal region

Figure 4.2: The composition of the signal regions, a) $q\bar{q}$ signal region and b) VBF signal region.

In table B.1, the list of summary of background MC simulation samples.

4.3 Study and Optimization of WZ QCD production in the VBF Control region

The QCD production of WZ is the main background in the VBF Signal Region (figure 4.1b). A recently published VBS and VBF analysis has shown a mismodelling of the QCD by the generators. That is an encouragement to study the WZ QCD in VBF, the control region, specifically. A control region enriched with the WZ QCD was built in order to compare the MC modelling to the obtained data. In the previous analysis a control region already existed. Defined as:
($100 < Mjj < 500$ and separation in rapidity < 3.5)
In figures 4.3a, 4.3b and 4.3c, the distributions of M(jj), ΔY(jj) and M(WZ) are shown, respectively. It looks at low Mjj and extrapolates it to the high Mjj signal region. Since mismodelling in the high Mjj region was observed in other analyses, it is a priority to optimize this definition in this thesis and obtain better results.
Now, the new control region will be defined as:
($100 < Mjj < 500$ Or separation in rapidity < 3.5)
In figures 4.4a, 4.4b and 4.4c, the distributions of M(jj), ΔY(jj) and M(WZ) are shown, respectively. Some events are now in the high Mjj >500 GeV region 4.4a, but low statistics. Data is $\simeq 15\%$ below the data in the high Mjj region. The table 4.5 presents the Data/MC yields in the WZ QCD control regions. Some events clearly manifest in the new VBS control region.

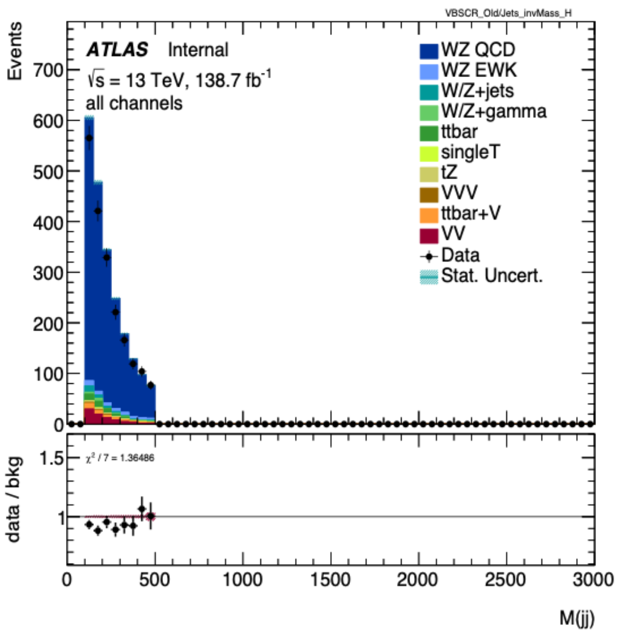

(a) Distribution of M(jj)

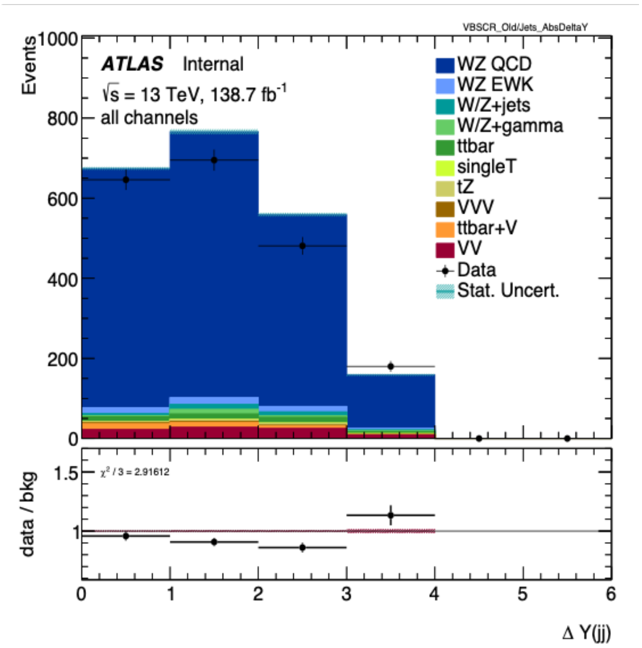

(b) Distribution of ΔY(jj)

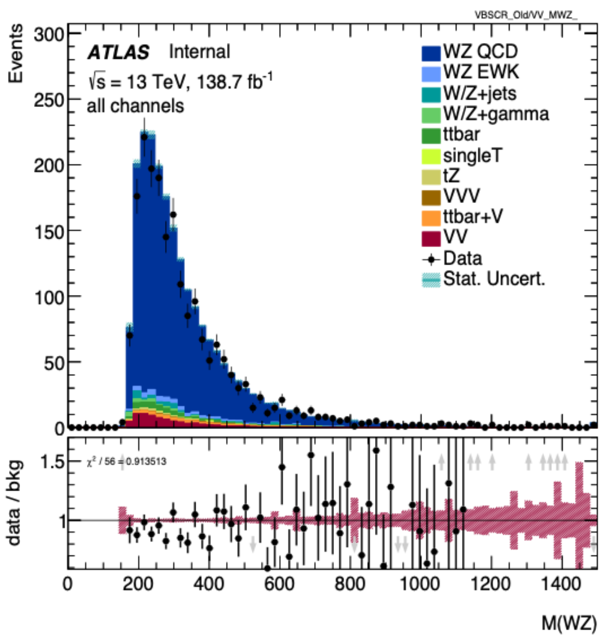

(c) Distribution of M(WZ)

Figure 4.3: The current VBF control region in: M(jj), ΔY(jj) and M(WZ) distributions.

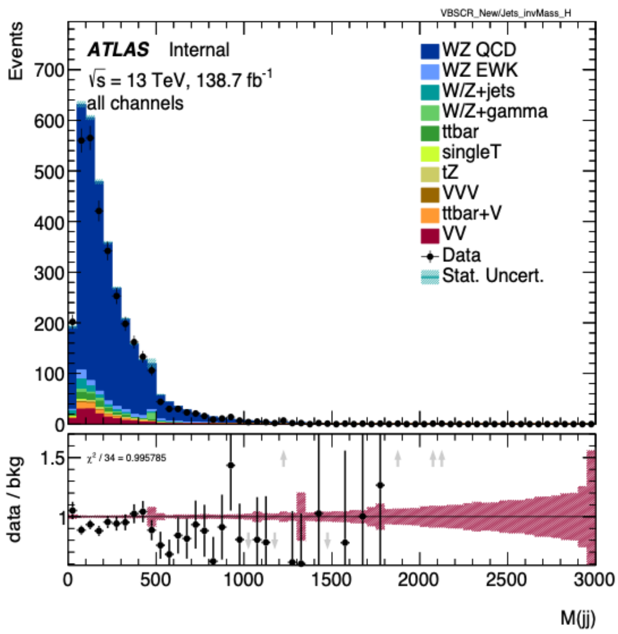

(a) Distribution of M(jj)

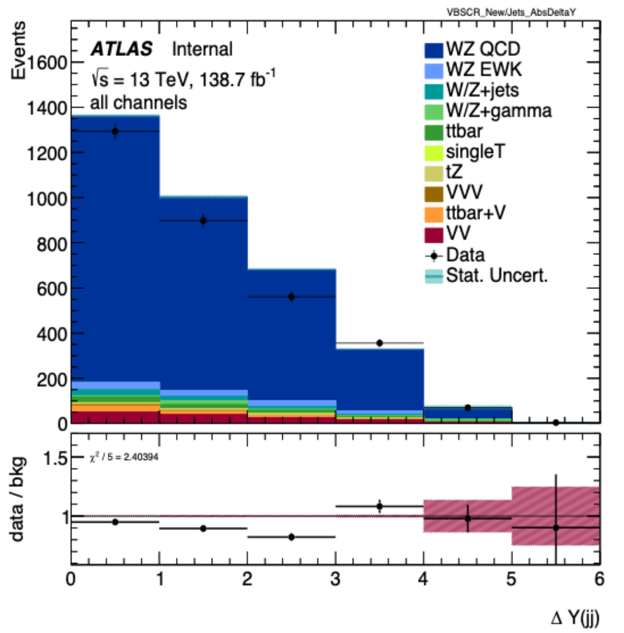

(b) Distribution of ΔY(jj)

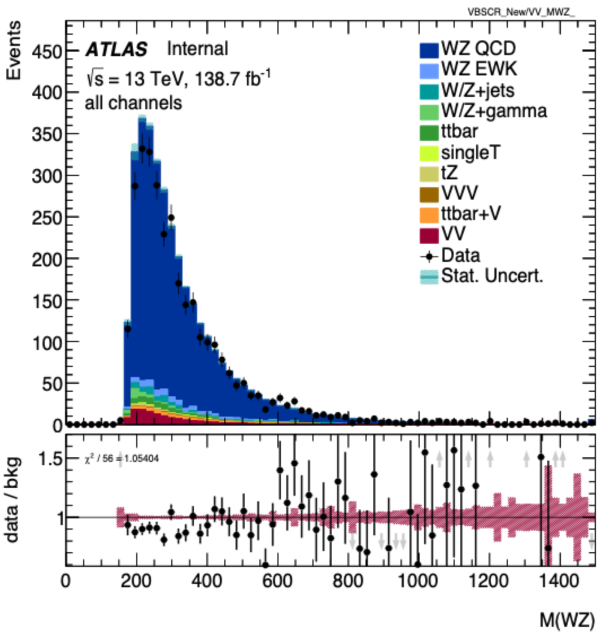

(c) Distribution of M(WZ)

Figure 4.4: The new VBF control region in: M(jj), ΔY(jj) and M(WZ) distributions.

VBFCR_current

		+/-
Data	2002	45
WZ QCD	1.873	4
WZ EWK	51	0,2
W/Z+jets	31	5
W/Z+gamma	19	5
ttbar	43	3
singleT	3	0,8
tZ	14	0,1
VVV	8	0,1
ttbar+V	33	0,4
VV	82	1
total BKG	2157,6	8,7

VBFCR_new

		+/-
Data	3182	56
WZ QCD	2944	6
WZ EWK	105	0,3
W/Z+jets	66	7,9
W/Z+gamm a	39	11,1
ttbar	68	3,3
singleT	8	1,3
tZ	22	0,14
VVV	13	0,16
ttbar+V	52	0,53
VV	135	1,4
total BKG	3452,2	15,3

Figure 4.5: Data/MC yields for the current and the new VBF control regions.

4.4 Background Fitting

As mentioned in the previous section, the major background of this analysis is the Standard Model WZ. For this background shape the analysis relies mainly on the MC simulation, which suffers from low statistics in the high mass tails. The possibility of describing the background with a fitted distribution is studied in this thesis in order to avoid fake bumps in the background distribution due to the MC statistics fluctuations.

This section is going to take a closer look at the description of the normalized distribution of the real "irreducible" background (WZ, ZZ, tZ and $t\bar{t}V$). The fit is carried out in regions where a search for new resonances should be performed ($m_{WZ} \in$ [300,3000*] GeV).

A signal of any new physics signal is likely to occur in the region of high WZ invariant mass m_{WZ}. In this case, this signal can minimize local fluctuations of the background (for instance in the high mass region). It is particularly important that the backgrounds in this region are well understood.

The empirical functional form 4.1 is used to describe the background shapes in both categories ($q\bar{q}$ and VBF) with different arameterizations found per signal region.

$$
\begin{aligned}
f_{q\bar{q}/VBF}(m_{WZ}) =& (f_1(m_{WZ}) + f_2(m_{WZ})) \times H(m_{WZ} - m_0) \times C_0 + f_3(m_{WZ}) \times H(m_0 - m_{WZ}) \\
& where: \\
& f_1(m_{WZ}) = \exp(a_1 + a_2 \cdot m_{WZ}) \\
& f_2(m_{WZ}) = (\frac{1}{2} + \frac{1}{2} erf(\frac{m_{WZ} - b_1}{b_2})) \times \frac{1}{1 + \exp(\frac{m_{WZ} - b_1}{b_3})} \\
& f_3(m_{WZ}) = \exp(c_1 + c_2 \cdot m_{WZ} + c_3 \cdot m_{WZ}^2 + c_4 \cdot m_{WZ}^{2.7}) \\
& \quad C_0 = \frac{f_3(m_0)}{f_1(m_0) + f_2(m_0)}
\end{aligned}
\tag{4.1}
$$

Moreover, separate fits of the reducible and irreducible backgrounds are used because of different kinematic behaviour of the two samples. However, the regions around the m_{WZ} peak and the higher mass region can be dealt with separatly.

The needful part of the equation 4.1 is f_3 because it describes the high mass tail. However f_1 describes the flat low mass region, and f_2 models the WZ threshold around the WZ mass. $H(x)$ is the Heaviside step function. it is used here to perform the transition between low and high mass parts around $m_0 = 400$ GeV. Finally, a_i, b_i and c_i are the shape parameters. These parameters will be fixed from MC fit for $q\bar{q}$ and VBF categories.

In figure 4.6, the distributions of WZ invariant mass fit projection of the background samples from the previous analysis are shown, figure 4.6a for $q\bar{q}$ and figure 4.6b for VBF categories, and the green band represents the fit uncertainties.

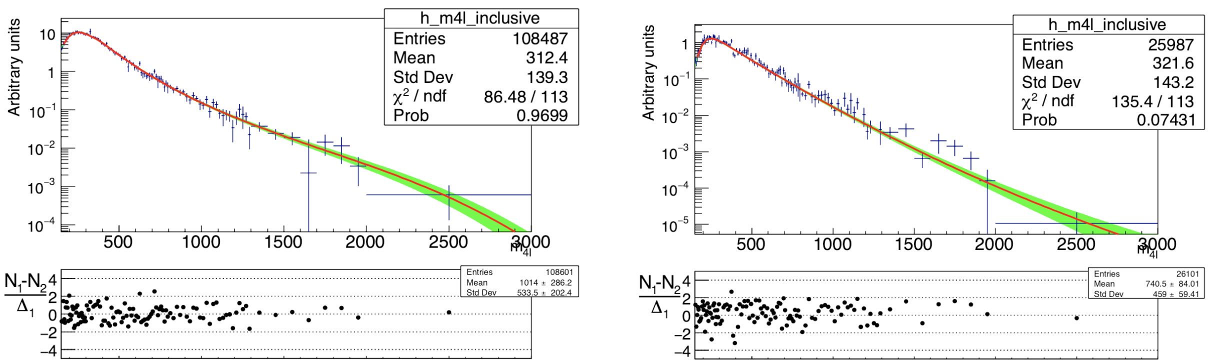

(a) qq category

(b) VBF category

Figure 4.6: Distributions of WZ invariant mass fit of the background samples in (a) $q\bar{q}$ and (b) VBF categories [2].

It is important to mention that the quality of the background shape fit is controlled by the terms $\chi^2 \setminus NDF$. This value ($\chi^2 \setminus NDF$) is around 1.2 for both categories that demonstrate a good compatibility of the model and the MC distribution.

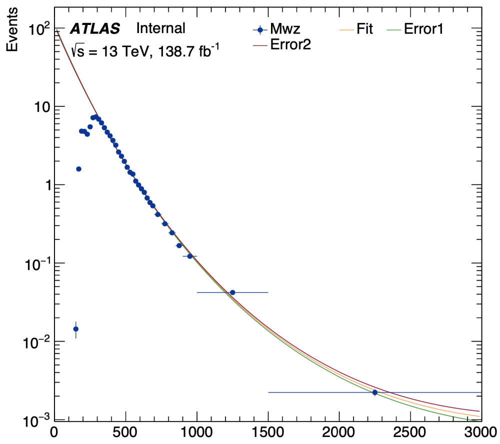

(a) Sherpa

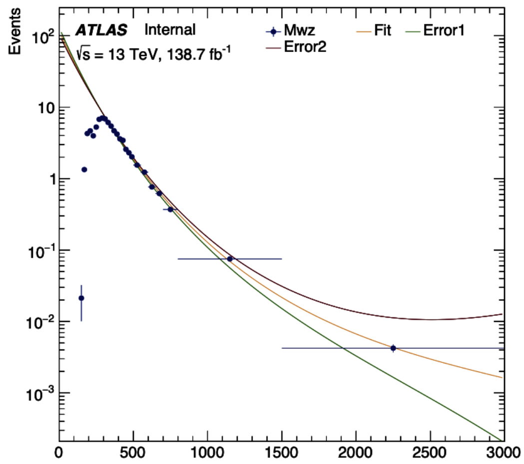

(b) Madgraph

Figure 4.7: Distributions of WZ invariant mass fit of the background samples in $q\bar{q}$ category.

In this thesis, the fit was performed from $m_{WZ} = 400$ GeV to simplify the process and focus on the description of the high mass tail. Figure 4.7 demonstrates the distributions of WZ invariant mass fit of the background samples in $q\bar{q}$ category. Two different MC generators are used to produce the WZ samples. Figure 4.7a and figure 4.7b show the samples produced by Sherpa and by the Madgraph MC generator, respectively.

PARAMETER	VALUE	ERROR	UNIT
C1	4.7	0.12	-
C2	-10	0.6	GeV^{-1}
C3	11	3.8	GeV^{-2}
C4	-8.4	3.3	$GeV^{-2.1}$

(a) Sherpa samples

PARAMETER	VALUE	ERROR	UNIT
C1	4.7	0.11	-
C2	-10	0.6	GeV^{-1}
C3	16	3.3	GeV^{-2}
C4	-12.7	3	$GeV^{-2.1}$

(b) Madgraph samples

Table 4.2: Tables of the fit parameter values of the function f_3. The fit is performed in the qq category. Table (a) contains the parameter values of the WZ samples produced by Sherpa, Table (b)- the Madgraph samples.

The fit uncertainty is indicated by the error lines (Error1 and Error2). There are different parameter values for each m_{WZ} distribution. The fit parameter values of the f_3 function are shown in the table 4.2 in the $q\bar{q}$ category. Table 4.2a contains the WZ sample that was produced by Sherpa and table 4.2b is for the WZ sample that produced by Madgraph. $\chi^2 \setminus NDF$ equals 3.1 for WZ Sherpa samples and 2.3 for WZ Madgraph samples in $q\bar{q}$ category.
The same process is carried out in the VBF category. Figure 4.8 contains the distributions of WZ invariant mass fit of the background samples in the VBF category. Two different MC generators are used to produce the WZ samples. Figure 4.8a contains the samples produced by Sherpa, figure 4.8b-by the Madgraph MC generator. The fit parameter values of the f_3 function are shown in the table 4.3 for the VBF category. Table 4.3a contains the WZ sample that

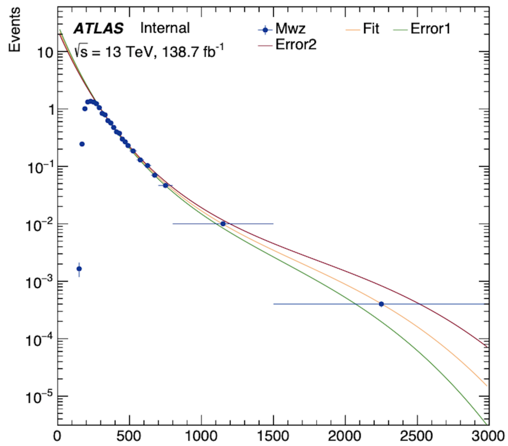

(a) Sherpa

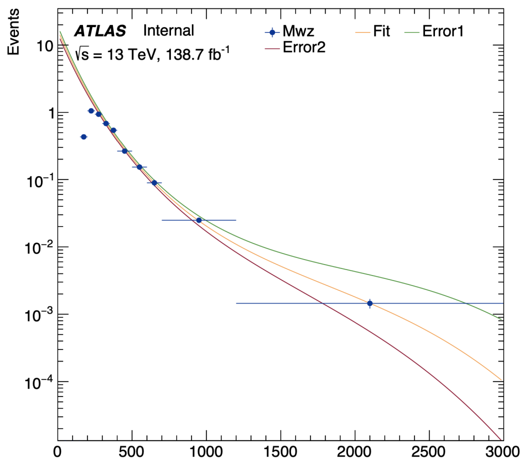

(b) Madgraph

Figure 4.8: Distributions of WZ invariant mass fit of the background samples in VBF.

produced by Sherpa. Table 4.3b contains the WZ sample produced by Madgraph. $\chi^2 \setminus NDF$ equals 1.1 for WZ Sherpa samples and 1.3 for WZ Madgraph samples in the VBF category.

PARAMETER	VALUE	ERROR	UNIT
C1	3.3	0.11	-
C2	-13	0.5	GeV^{-1}
C3	37	3.7	GeV^{-2}
C4	-30	2.7	$GeV^{-2.1}$

(a) Sherpa samples

PARAMETER	VALUE	ERROR	UNIT
C1	2.8	0.13	-
C2	-12.6	0.3	GeV^{-1}
C3	31	0.9	GeV^{-2}
C4	-26	0.5	$GeV^{-2.1}$

(b) Madgraph samples

Table 4.3: Tables of the fit parameter values of the function f_3. The fit is performed in VBF category. Table (a) contains the parameter values of the WZ samples produced by Sherpa and Table (b) - the Madgraph samples.

Finally, the first studies about the modelling of the WZ background were shown in this section. To improve the background description in the tail of the distribution a fit of the WZ irreducible background was performed. Systematics studies on the fitted function still need to be done by the following: find a different function (more stable) to describe the tail, do spurious signal studies using some benchmark models and calculate systematics uncertainties for this approach.

4.5 MC generator comparison

In High Energy Physics, nothing is performed without certainty and without considering the potential consequences of the collision. Therefore, in all collision experiments such as the ones in the LHC, the usage of a simulation system is essential. In LHC, parts that are responsible for production of events are called Monte Carlo event generators: Pythia, Sherpa, Madgraph,

POWHEG, MG5_aMC@NLO and Herwig.
Two MC generators—Sherpa and Madgraph—are going to be compared in the following paragraphs. They can be used for modelling the WZ process. Figure 4.9 shows a comparison of WZ

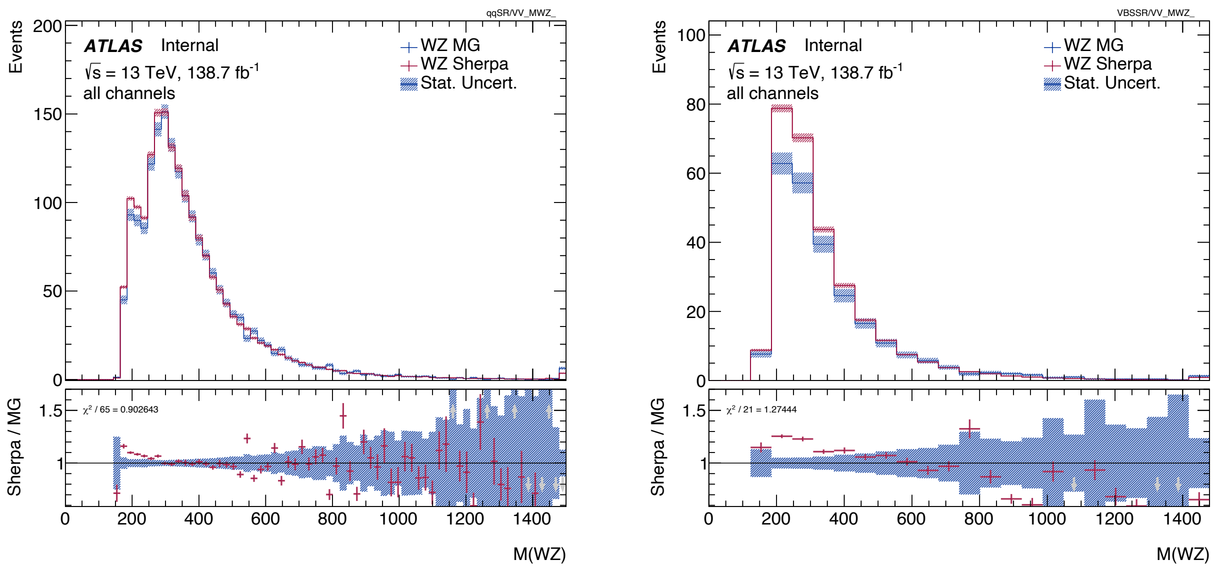

(a) qq signal region

(b) VBF signal region

Figure 4.9: Comparison of the WZ (QCD+EWK) predictions in the two signal regions.

	qq	VBS
WZ Sherpa	1828 ± 8	285 ± 2
WZ Madgraph	1794 ± 15	249 ± 6

Table 4.4: Comparison of the WZ (QCD+EWK) predictions in the two signal regions.

(QCD+EWK) predictions in two signal regions-qq(a) and VBF(b). The blue shape represents the WZ production generated by Madgraph, the red shape-Sherpa generator. Differences in the shapes of the distributions are clearly visible, especially at low M (WZ). Table 4.4 presents the number of events in each signal region. The next sections are going to describe the differences between Madgraph and Sherpa in (QCD and EWK) WZ production to check if the MC samples match the actual data.

4.5.1 Comparison of the predictions given by Madgraph and Sherpa in (qq and VBF) signal regions for WZ-QCD production

Figure 4.10 demonstrates a comparison of the WZ-QCD predictions in the two signal regions-qq(a and b) and VBF(c and d). This comparison is made in the WZ invariant mass m_{WZ} distribution and the distribution of m_{jj}. The blue shape represents the WZ production generated by Madgraph, the red shape—by Sherpa. Differences in the shapes of the distributions are obvious, and they are especially noticeable in the VBS region. The reason for this difference is that Sherpa includes 3rd jet at Leading order, but Madgraph does not. Table 4.5 depicts the number of events in each signal region.

	qq	VBS
WZ QCD Sherpa	1794 ± 8	242 ± 2
WZ QCD Madgraph	1759 ± 15	182 ± 6

Table 4.5: Comparison of the WZ-QCD prediction in the qq and VBF signal regions. Same WZ-QCD samples produced by different MC generators.

4.5.2 Comparison of the predictions given by Madgraph and Sherpa in (qq and VBF) signal regions for WZ-EWK production

In the previous section, the comparison was made between Sherpa and Madgraph in the WZ-QCD production in qq and VBF signal regions. In this section, Sherpa and Madgraph will be compared in qq and VBF signal regions but for the WZ-EWK production. Figure 4.12 depicts a comparison of the WZ-EWK predictions in the two signal regions-qq(a and b) and VBF(c and d). This comparison is made in two distributions-WZ invariant mass m_{WZ} and the distribution of m_{WZ}.
The blue shape represents the WZ production given by Madgraph generator and the red shape-Sherpa generator. Difference in the shapes of the distributions (m_{WZ} and m_{WZ}) are obvious, especially in the VBS region. This differences is due to a color bug in the Sherpa generator. The table 4.6 shows the number of events in each signal region.

	qq	VBS
WZ EWK Sherpa	33.62 ± 0.19	42.69 ± 0.21
WZ EWK Madgraph	35.32 ± 0.26	66.3 ± 0.4

Table 4.6: Comparison of the WZ-EWK prediction in the qq and VBF signal regions. Same WZ-EWK samples produced by different MC generators.

Finally, a large discrepancy (∼50%) appears at the level of the delta rapidity between the jets cut. Cutflow comparison 4.11 obviously shows the region which keeps with the Delta eta cut is the one with the largest mismodelling.

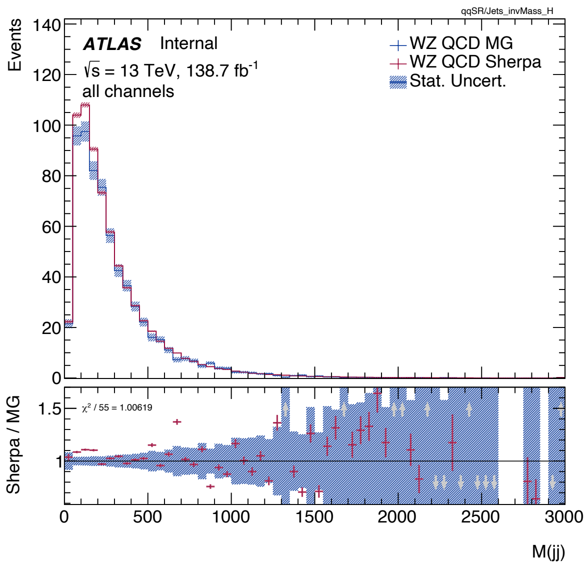

(a) m_{jj} distribution in qq signal region.

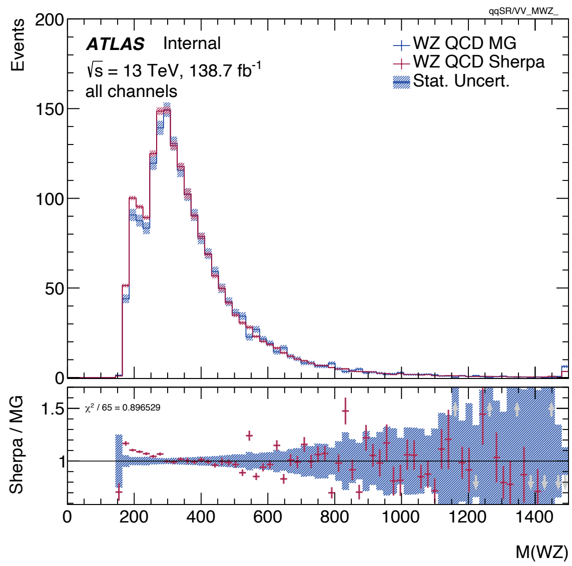

(b) m_{WZ} distribution in qq signal region.

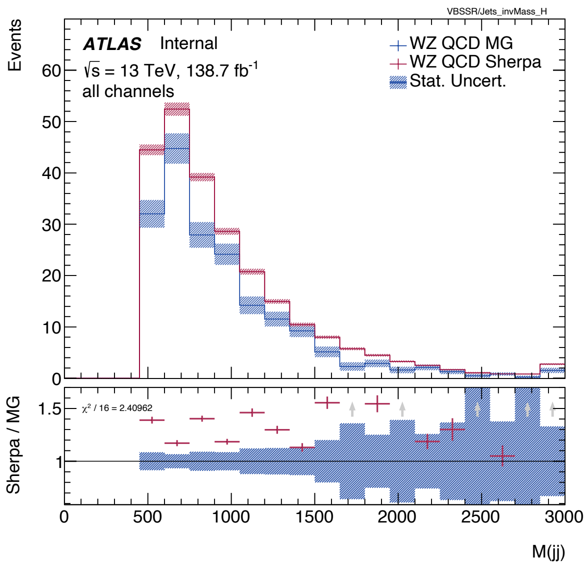

(c) m_{jj} distribution in VBF signal region.

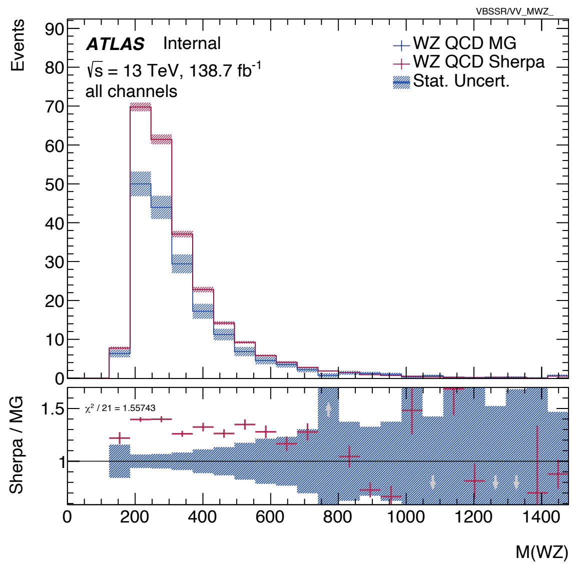

(d) m_{WZ} distribution in VBF signal region.

Figure 4.10: Comparison of the predictions given by Madgraph and Sherpa in the qq and VBF signal regions for the WZ-QCD prediction.

	WZ EWK Sherpa	WZ EWK MG
inclusive	213.1 ± 0.5	241.7 ± 0.7
N_jet	170.4 ± 0.4	195.7 ± 0.6
TaggingJets	170.4 ± 0.4	195.7 ± 0.6
Jet_cut	170.4 ± 0.4	195.7 ± 0.6
bVeto	142.4 ± 0.4	164.6 ± 0.6
Rapidity cut	45.94 ± 0.22	70.0 ± 0.4
VBFSR	42.69 ± 0.21	66.3 ± 0.4

~15% difference

~50% difference

Figure 4.11: The cutflow comparison between Sherpa and MG for WZ-EWK production.

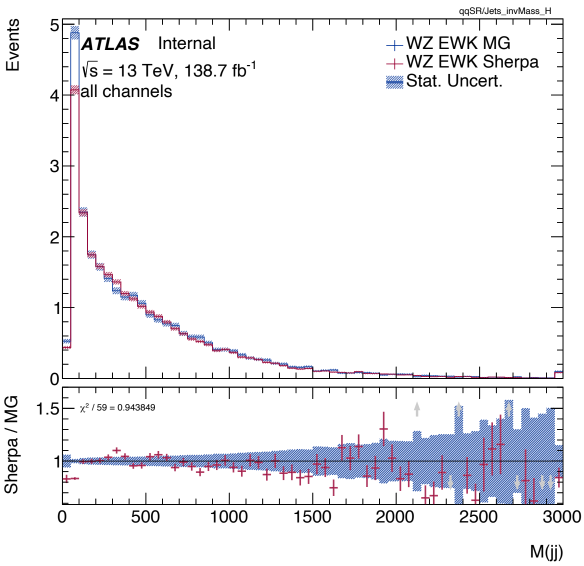

(a) m_{jj} distribution in qq signal region.

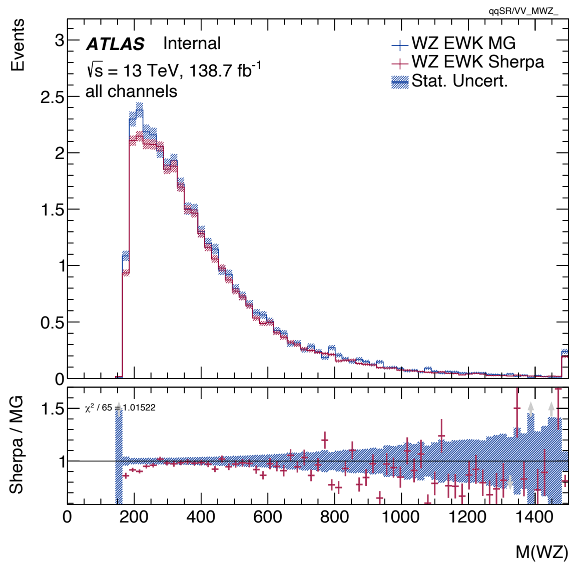

(b) m_{WZ} distribution in qq signal region.

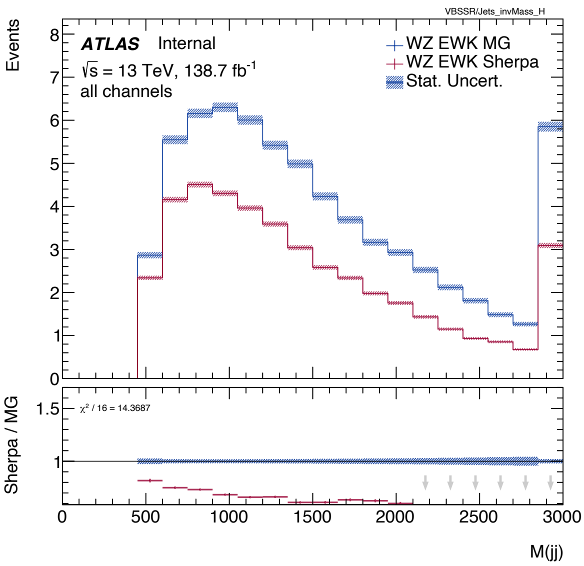

(c) m_{jj} distribution in VBF signal region.

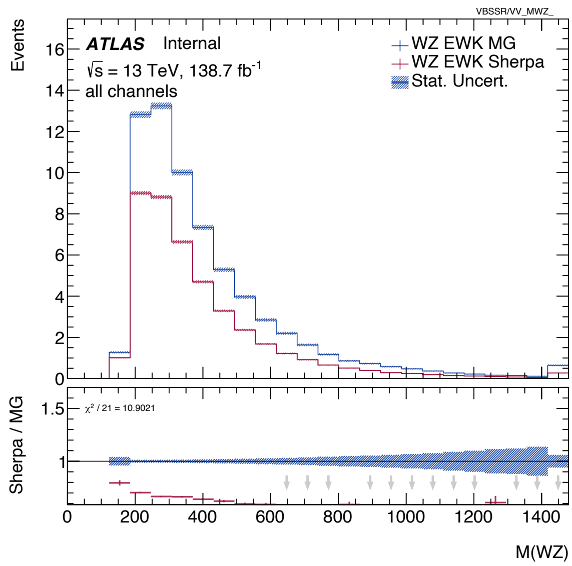

(d) m_{WZ} distribution in VBF signal region.

Figure 4.12: comparison of the predictions given by Madgraph and Sherpa in the qq and VBF signal regions for the WZ-EWK prediction.

4.6 WZ reweighing studies

Currently, the VBF-cut based control region is defined by the following selection criteria: the di-jet invariant mass to be $100 < M_{jj} < 500$ GeV and $| \triangle Y_{jj}| < 3.5$. Figure 4.13 shows the invariant mass distribution for this VBF control region. It can be clearly noticed that this VBF control region contains a small contamination from ZZ and other irreducible background processes besides the $W^{\pm}Z$ events.

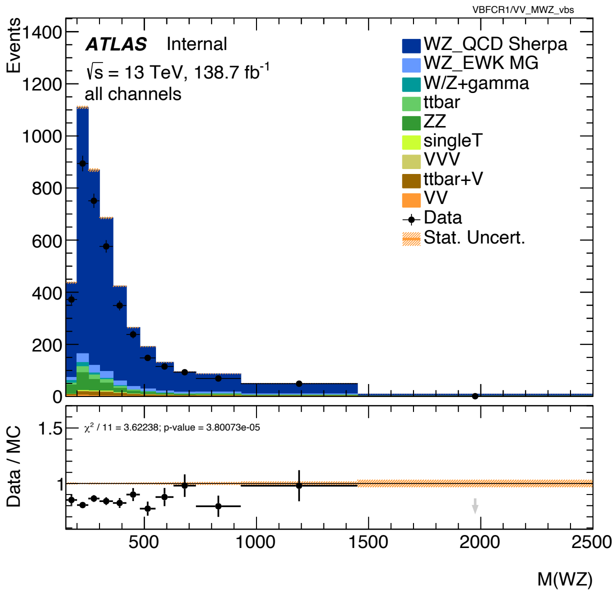

Figure 4.13: The invariant mass distribution for the VBF control region.

Moreover, this VBF control region obviously shows a mismodelling, specifically for the low $W^{\pm}Z$ invariant mass. Fortunately, the modelling will be later corrected in the fit. Also, the modelling is fully covered by the theory of systematic uncertainties. It equals $\simeq 30\%$ for the WZ QCD in this VBF control region.

In the next steps, two extra definitions of the VBF control region will be given and compared with the current definition. This comparison can provide a deep understanding of the VBF phase space and can potentially be used to correct the mismodelling for the low $W^{\pm}Z$ invariant mass.

The definition of the current VBF control region will be labelled as VBFCR1, and the other two definitions will be labelled as VBFCR2 and VBFCR3. They are defined as follows:

- VBFCR1 $\Rightarrow$ ($100 < M_{jj} < 500$ GeV) OR ($| \triangle Y_{jj}| < 3.5$)
- VBFCR2 $\Rightarrow$ ($100 < M_{jj} < 500$ GeV) OR (Z_Centrality > 0.4)
- VBFCR3 $\Rightarrow$
  ($100 < M_{jj} < 500$ GeV) OR ($| \triangle Y_{jj}| < 3.5$) OR (Z_Centrality > 0.4)

Here, M_{jj} is the di-jet invariant mass, $\triangle Y_{jj}$ is the rapidity separation and $Z\_Centrality$ is the centrality.

4.6.1 Compare between Sherpa and Madgraph in 3 the different definitions of VBF-control regions

The WZ-QCD Monte Carlo samples can be produced by two different generators-Sherpa and Madgraph, of course, with various properties and uncertainties. This section shows a comparison between the WZ QCD samples produced by Sherpa and the WZ-QCD samples produced by Madgraph with data collected from the full Run 2 (2015-2018). This comparison is performed in the three different VBF control regions that were defined in the previous sections.

4.6.1.1 VBFCR1, VBFCR2 and VBFCR3

The VBFCR1 is defined as (VBFCR1 $\Rightarrow$ ($100 < M_{jj} < 500$ GeV) OR ($| \triangle Y_{jj}| < 3.5$). Figure 4.14 shows the distributions of m_{jj} in VBFCR1 for the data/MC comparison, with different bin widths. The MC samples are produced by the two generators (Sherpa and Madgraph). Table 4.7 shows the number of events for the data/MC comparison of Sherpa and Madgraph in VBFCR1. Figures 4.15 depicts the data-MC(All MC but not WZ QCD) comparison of Sherpa and Madgraph for VBFCR1. Table 4.8 shows the number of events in this comparison. The same procedure is carried out for VBFCR2 and VBFCR3. The comparisons between data and MC in VBFCR2 and VBFCR3 are shown in the following figures and tables.

	Data	WZ_QCD	WZ_EWK MG	W/Z+gamma	ttbar	ZZ	singleT	VVV	VV	total BKG
VBFCR1 Sherpa	3660 ± 60	3710 ± 9	168.3 ± 0.6	47 ± 5	80 ± 3	226 ± 1	11 ± 1	15.09 ± 0.18	13.97 ± 0.10	4272 ± 11
VBFCR1 MG	3660 ± 60	3652 ± 13	168.3 ± 0.6	47 ± 5	80 ± 3	226 ± 1	11 ± 1	15.09 ± 0.18	13.97 ± 0.10	4214 ± 14

Table 4.7: The data/MC comparison of Sherpa and MG for VBFCR1.

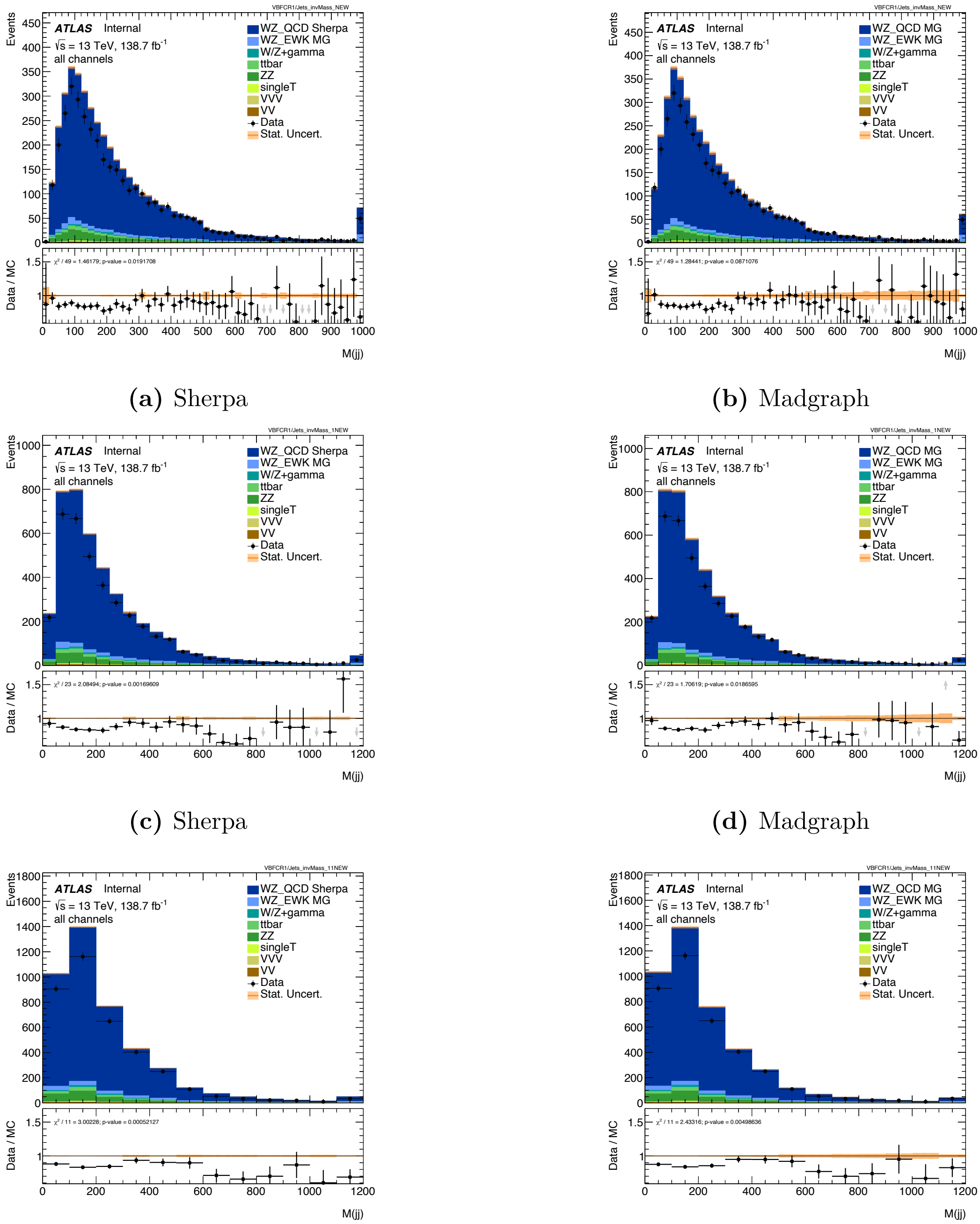

(a) Sherpa (b) Madgraph

(c) Sherpa (d) Madgraph

(e) Sherpa (f) Madgraph

Figure 4.14: Distributions of m_{jj} in VBFCR1 for the data/MC comparison, with different bin widths. MC samples produced by two generators (Sherpa and Madgraph).

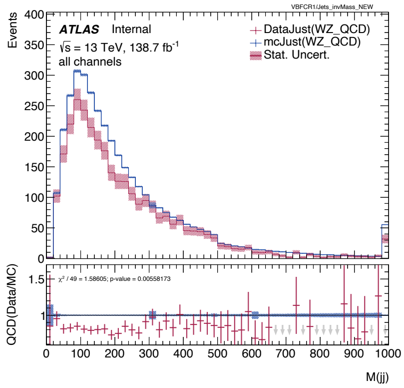

(a) Sherpa

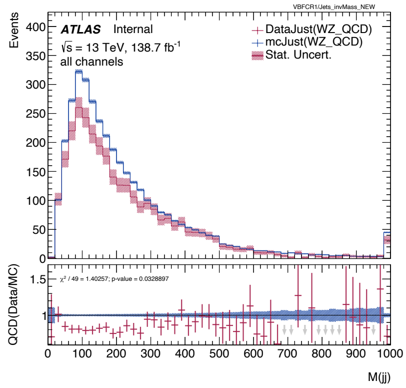

(b) Madgraph

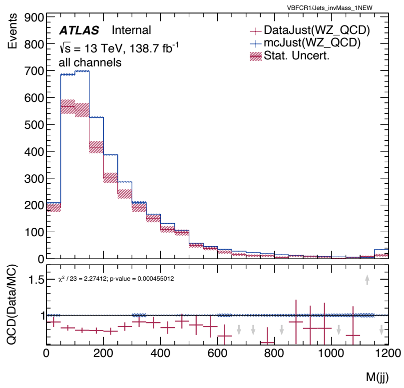

(c) Sherpa

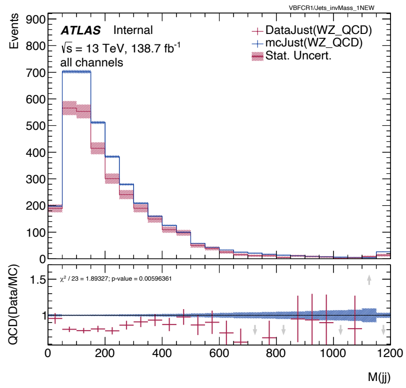

(d) Madgraph

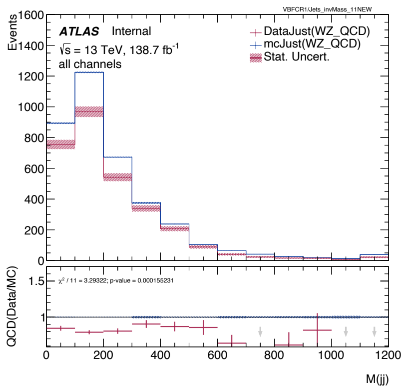

(e) Sherpa

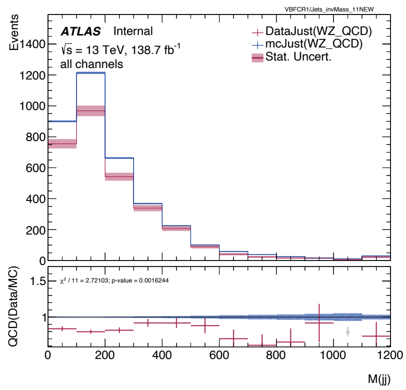

(f) Madgraph

Figure 4.15: The data-MC(All MC but not WZ QCD) comparison of Sherpa and Madgraph for VBFCR1.

	DataJust(WZ_QCD)	mcJust(WZ_QCD)
VBFCR1 Sherpa	3020 ± 60	3710 ± 9
VBFCR1 MG	3020 ± 60	3652 ± 13

Table 4.8: The data-MC(All MC but not WZ QCD) comparison of Sherpa and Madgraph for VBFCR1.

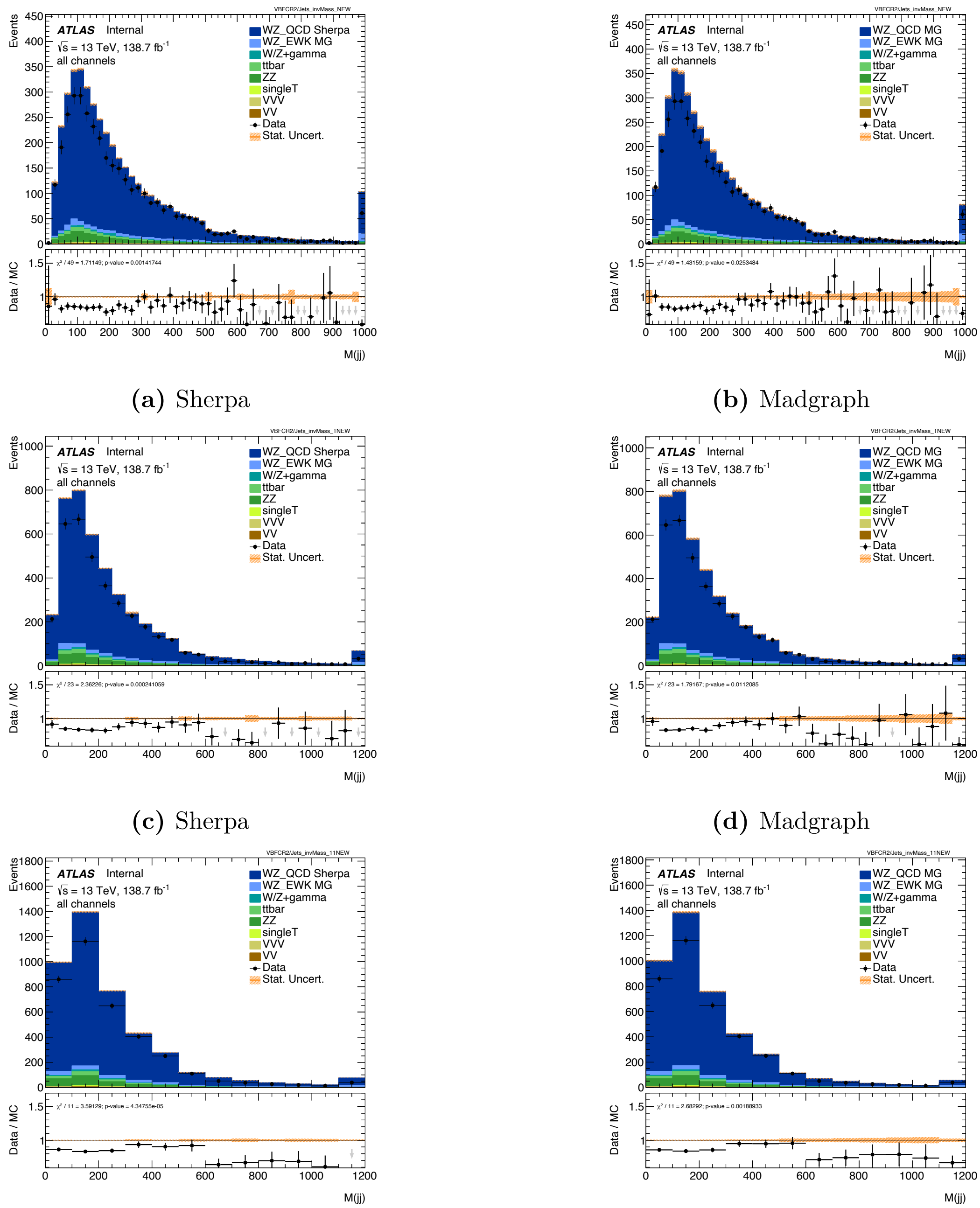

(a) Sherpa **(b)** Madgraph

(c) Sherpa **(d)** Madgraph

(e) Sherpa **(f)** Madgraph

Figure 4.16: Distributions of m_{jj} in VBFCR2 for the data/MC comparison, with different bin widths. MC samples produced by two generators (Sherpa and Madgraph).

	Data	WZ_QCD	WZ_EWK MG	W/Z+gamma	ttbar	ZZ	singleT	VVV	VV	total BKG
VBFCR2 Sherpa	3620 ± 60	3731 ± 9	165.3 ± 0.6	47 ± 5	80 ± 3	227 ± 1	11 ± 1	14.91 ± 0.18	14.13 ± 0.10	4290 ± 11
VBFCR2 MG	3620 ± 60	3650 ± 13	165.3 ± 0.6	47 ± 5	80 ± 3	227 ± 1	11 ± 1	14.91 ± 0.18	14.13 ± 0.10	4209 ± 14

Table 4.9: The data/MC comparison of Sherpa and MG for VBFCR2.

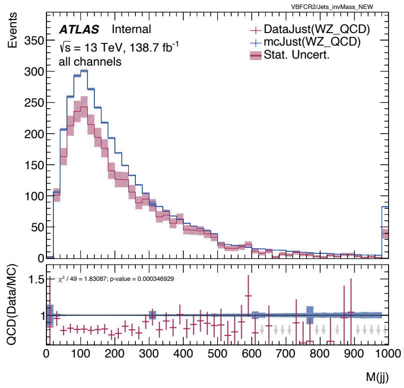

(a) Sherpa

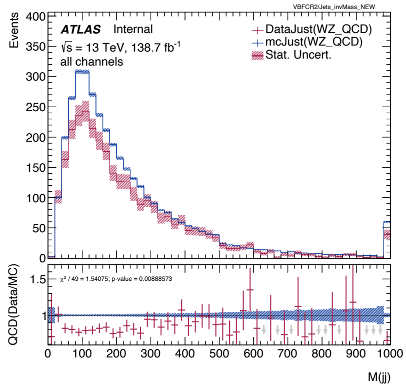

(b) Madgraph

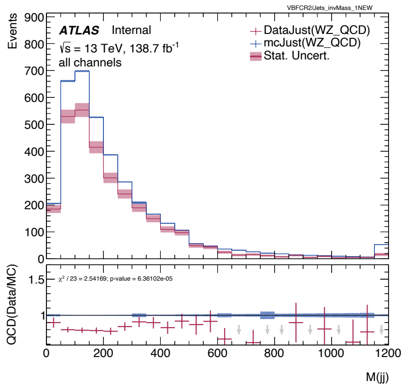

(c) Sherpa

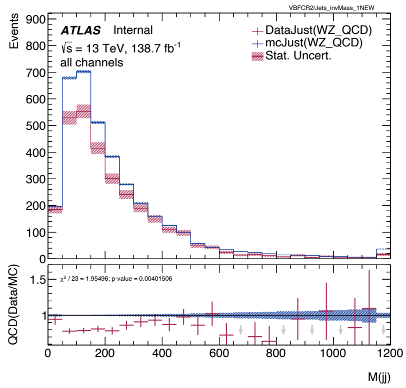

(d) Madgraph

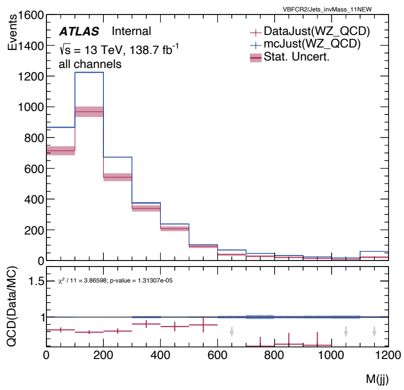

(e) Sherpa

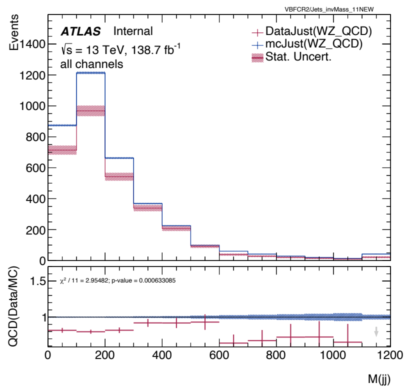

(f) Madgraph

Figure 4.17: The data-MC(All MC but not WZ QCD) comparison of Sherpa and Madgraph for VBFCR2.

	DataJust(WZ_QCD)	mcJust(WZ_QCD)
VBFCR2 Sherpa	3000 ± 60	3731 ± 9
VBFCR2 MG	3000 ± 60	3650 ± 13

Table 4.10: The data-MC(All MC but not WZ QCD) comparison of Sherpa and Madgraph for VBFCR2.

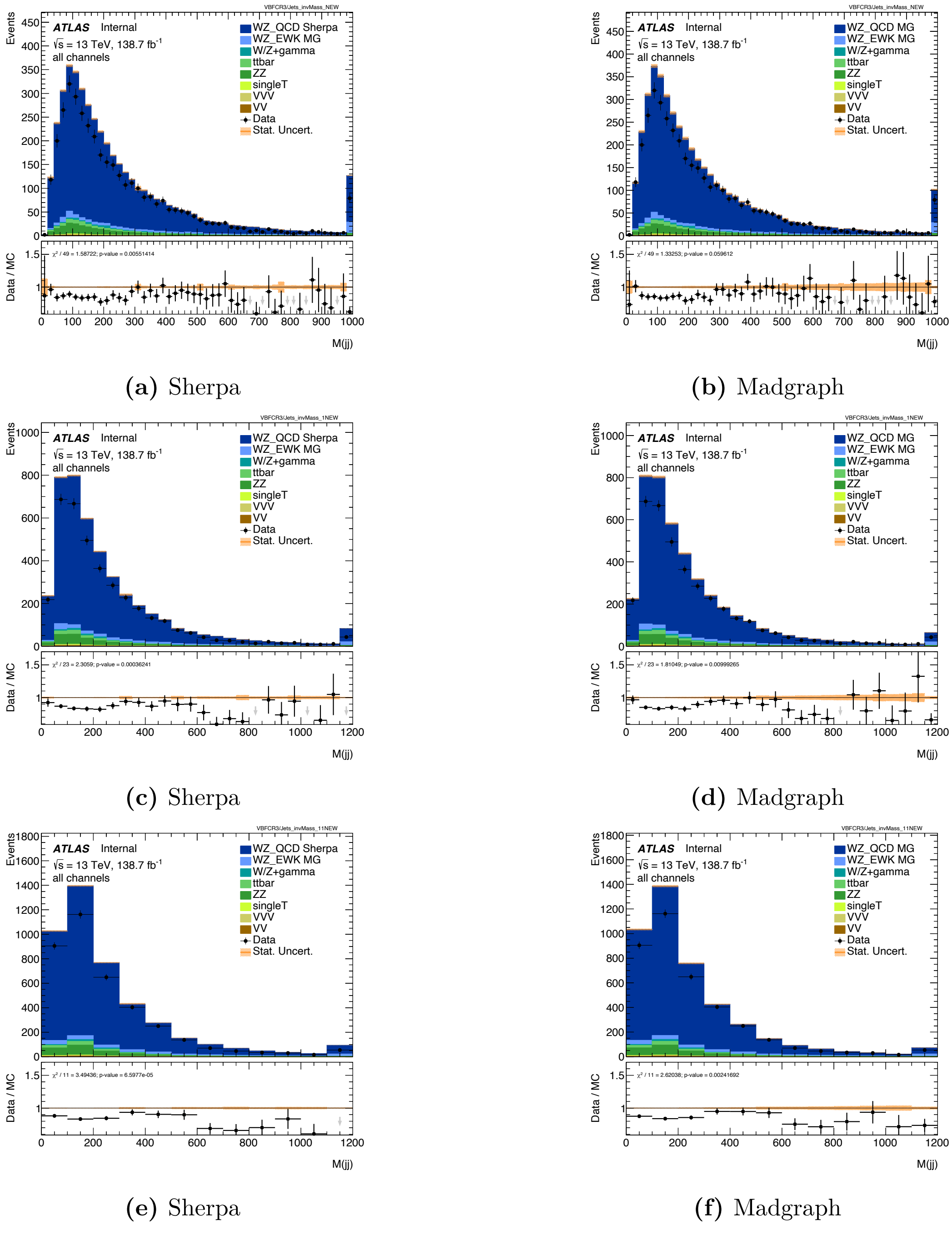

(a) Sherpa (b) Madgraph

(c) Sherpa (d) Madgraph

(e) Sherpa (f) Madgraph

Figure 4.18: Distributions of m_{jj} in VBFCR3 for the data/MC comparison, with different bin widths. MC samples produced by two generators (Sherpa and Madgraph).

	Data	WZ_QCD	WZ_EWK MG	W/Z+gamma	ttbar	ZZ	singleT	VVV	VV	total BKG
VBFCR3 Sherpa	3760 ± 60	3839 ± 9	186.5 ± 0.6	49 ± 5	81 ± 3	232 ± 1	11 ± 1	15.43 ± 0.18	14.40 ± 0.10	4429 ± 11
VBFCR3 MG	3760 ± 60	3753 ± 13	186.5 ± 0.6	49 ± 5	81 ± 3	232 ± 1	11 ± 1	15.43 ± 0.18	14.40 ± 0.10	4343 ± 14

Table 4.11: The data/MC comparison of Sherpa and MG for VBFCR3.

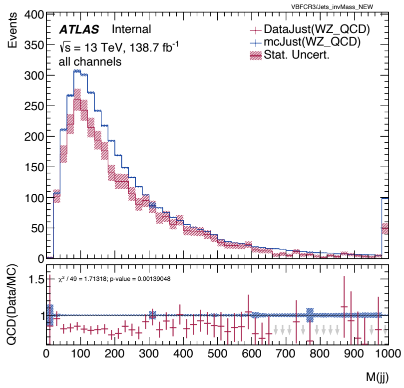

(a) Sherpa

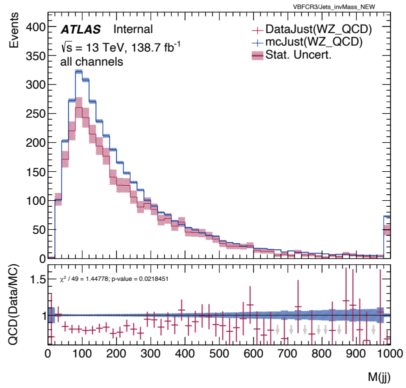

(b) Madgraph

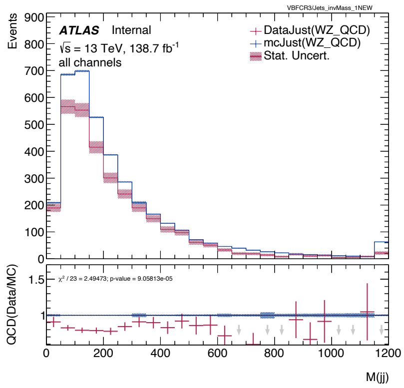

(c) Sherpa

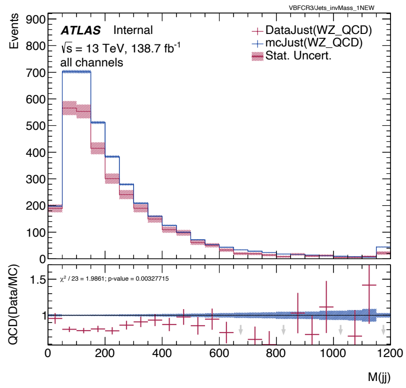

(d) Madgraph

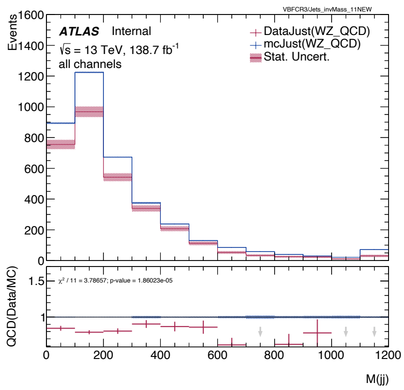

(e) Sherpa

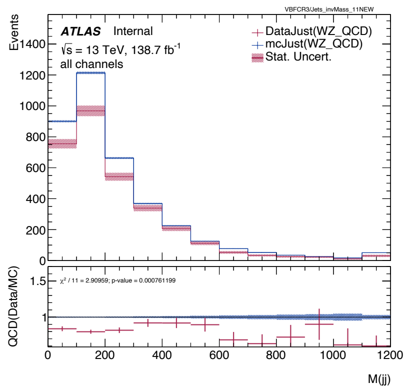

(f) Madgraph

Figure 4.19: The data-MC(All MC but not WZ QCD) comparison of Sherpa and Madgraph for VBFCR3.

	DataJust(WZ_QCD)	mcJust(WZ_QCD)
VBFCR3 Sherpa	3100 ± 60	3839 ± 9
VBFCR3 MG	3100 ± 60	3753 ± 13

Table 4.12: The data-MC(All MC but not WZ QCD) comparison of Sherpa and Madgraph for VBFCR3.

4.7 WZ reweighing results

Figures 4.20 demonstrates the WZ invariant mass distributions in the three VBF control regions (VBFCR1, VBFCR2 and VBFCR3). The control regions studied here sparked a discussions at CERN about the validity of the control region CR being used in the analysis. However, the CR1 was actually implemented in the nominal ATLAS collaboration analysis. Due to a bias in the M_{jj} distribution of CR1 between high (>500 GeV) and low (<500 GeV) M_{jj}, only the high M_{jj} part of the region will be used for the publication.

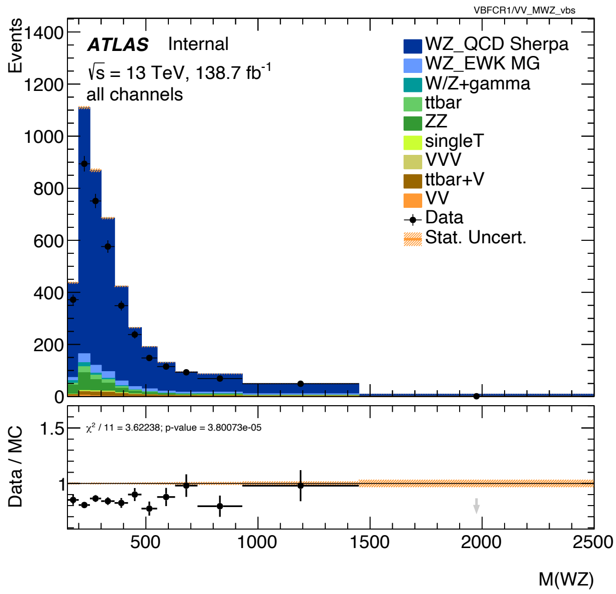

(a) VBFCR1

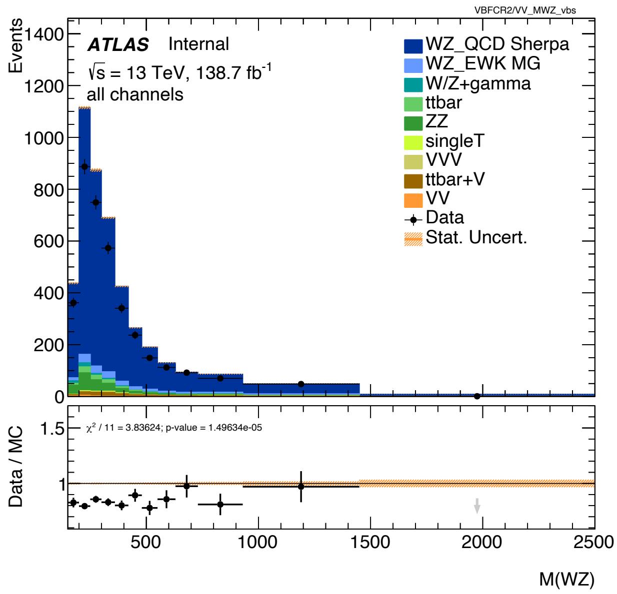

(b) VBFCR2

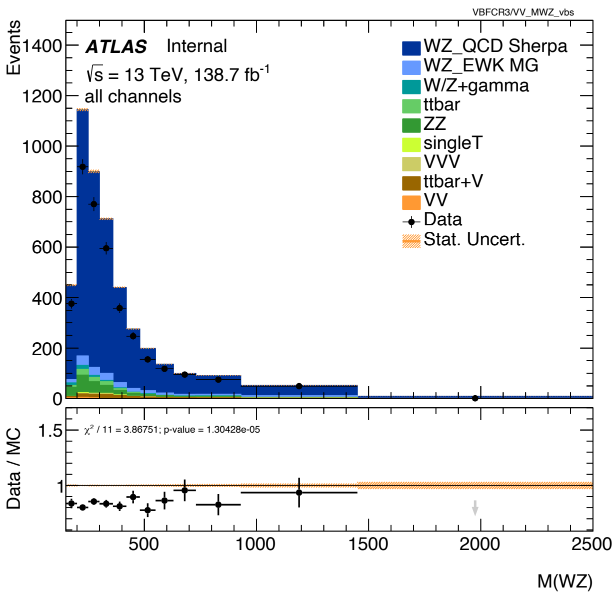

(c) VBFCR3

Figure 4.20: The WZ invariant mass distributions of the three VBF control regions.

5 Conclusion

In conclusion, resonance searches are the easiest way to find new physics. To put it simply, the essence of the method is to look for an excess over a well known background. Knowing the SM background with small uncertainties is crucial to actually be able to see an excess.
This work is focused on checking the modeling of the main background; in this analysis, the background is WZ SM. Several possibilities for this background have been studied: first, in order to avoid the MC statistics fluctuations in the tail, a fit has been implemented to smooth the distribution. The idea is to apply this fit directly to the data.
Secondly, 2 MC generators were compared to ensure that the predicted MC shape is correct. Since some differences were noticed, they were added to the uncertainties. A control region was created to extract the normalization of the background while keeping the shape predicted by the MC (here, several possibilities were studied, and the analysis team chose one of them). Finally, the MC is reweighted according to the data in the CR to correct the shape mismodelling.

A Mathematical Definition

A.1 Pauli Matrices and another important Matrices

$$\sigma_x = \begin{pmatrix} 0 & 1 \\ 1 & 0 \end{pmatrix}, \sigma_y = \begin{pmatrix} 0 & -i \\ i & 0 \end{pmatrix}, \sigma_z = \begin{pmatrix} 1 & 0 \\ 0 & -1 \end{pmatrix} \tag{A.1}$$

$$\gamma^0 = \begin{pmatrix} 1 & 0 & 0 & 0 \\ 0 & 1 & 0 & 0 \\ 0 & 0 & -1 & 0 \\ 0 & 0 & 0 & -1 \end{pmatrix}, \gamma^1 = \begin{pmatrix} 0 & 0 & 0 & 1 \\ 0 & 0 & 1 & 0 \\ 0 & -1 & 0 & 0 \\ -1 & 0 & 0 & 0 \end{pmatrix}, \gamma^2 = \begin{pmatrix} 0 & 0 & 0 & -i \\ 0 & 0 & i & 0 \\ 0 & i & 0 & 0 \\ -i & 0 & 0 & 0 \end{pmatrix}, \gamma^3 = \begin{pmatrix} 0 & 0 & 1 & 0 \\ 0 & 0 & 0 & -1 \\ -1 & 0 & 0 & 0 \\ 0 & 1 & 0 & 0 \end{pmatrix} \tag{A.2}$$

$$\gamma^5 = i\gamma^0\gamma^1\gamma^2\gamma^3 = \begin{pmatrix} 0 & 0 & 1 & 0 \\ 0 & 0 & 0 & 1 \\ 1 & 0 & 0 & 0 \\ 0 & 1 & 0 & 0 \end{pmatrix} \tag{A.3}$$

B Samples

B.1 The list of summary of background MC simulation samples

DSID	Background	MC-Generators	PDF
364253	WZ QCD	Sherpa222	NNPDF30NNLO
361292	WZ QCD	MGaMcAtNloPy8EG	NNPDF30LO
364284	WZ EWK	Sherpa222	NNPDF30NNLO
364739	WZ EWK	MGaMcAtNloPy8EG	NNPDF30NLO
364740	WZ EWK	MGaMcAtNloPy8EG	NNPDF30NLO
364741	WZ EWK	MGaMcAtNloPy8EG	NNPDF30NLO
364742	WZ EWK	MGaMcAtNloPy8EG	NNPDF30NLO
361600	Powheg/VV	PowhegPy8EG	AZNLOCTEQ6L1
361603	Powheg/VV	PowhegPy8EG	AZNLOCTEQ6L1
361604	Powheg/VV	PowhegPy8EG	AZNLOCTEQ6L1
364250	Sherpa/VV	Sherpa222	NNPDF30NNLO
364254	Sherpa/VV	Sherpa222	NNPDF30NNLO
364283	Sherpa/VV	Sherpa222	NNPDF30NNLO
345705	Sherpa/gg	Sherpa222	NNPDF30NNLO
345706	Sherpa/gg	Sherpa222	NNPDF30NNLO
361100 - 361108	V+jets	PowhegPythia8EvtGen	AZNLOCTEQ6L1
410470	ttbar	PowhegPythia8EvtGen	A14 NNPDF23LO
410658	SingleTop	PowhegPythia8EvtGen	A14 NNPDF23LO
410659	SingleTop	PowhegPythia8EvtGen	A14 NNPDF23LO
410644 - 410649	SingleTop	PowhegPythia8EvtGen	A14 NNPDF23LO
410650	SingleTop	MadGraphPythia8EvtGen	A14 NNPDF23LO
410155	ttV	MadGraphPythia8EvtGen	A14N23LO
410218	ttV	MadGraphPythia8EvtGen	A14N23LO
410219	ttV	MadGraphPythia8EvtGen	A14N23LO
410220	ttV	MadGraphPythia8EvtGen	A14N23LO
364500 - 364514	Vgamma	Sherpa222	NNPDF30NNLO
364521 - 364535	Vgamma	Sherpa222	NNPDF30NNLO
364242 - 364249	Triboson	Sherpa222	NNPDF30NNLO

Table B.1: The list of summary of background MC simulation samples, STDM5 derivations for MC16a, MC16d and MC16e samples are used

List of Figures

List of Tables

Bibliography

[1] The physics hypertextbook. https://physics.info/standard/.

[2] Search for resonant wz production in run-2 of the lhc .... https://cds.cern.ch/record/2714128/files/ATL-COM-PHYS-2020-235.pdf.

[3] W boson: Sunshine and stardust. https://home.cern/science/physics/w-boson-sunshine-and-stardust.

[4] *ATLAS detector and physics performance: Technical Design Report, 1*. Technical Design Report ATLAS. CERN, Geneva, 1999.

[5] Standard Model Summary Plots Spring 2020. Technical report, CERN, Geneva, May 2020. All figures including auxiliary figures are available at https://atlas.web.cern.ch/Atlas/GROUPS/PHYSICS/PUBNOTES/ATL-PHYS-PUB-2020-010.

[6] Daniele Alves, Nima Arkani-Hamed, Sanjay Arora, Yang Bai, Matthew Baumgart, Joshua Berger, Matthew Buckley, Bart Butler, Spencer Chang, Hsin-Chia Cheng, and et al. Simplified models for lhc new physics searches. *Journal of Physics G: Nuclear and Particle Physics*, 39(10):105005, Sep 2012.

[7] Nima Arkani-Hamed, Andrew G Cohen, Emanuel Katz, and Ann E Nelson. The littlest higgs. *Journal of High Energy Physics*, 2002(07):034–034, Jul 2002.

[8] ATLAS Collaboration. The ATLAS Experiment at the CERN Large Hadron Collider. *JINST*, 3:S08003, 2008.

[9] Duarte Azevedo, Pedro Ferreira, Heather E. Logan, and Rui Santos. Vacuum structure of the z2 symmetric georgi-machacek model. *Journal of High Energy Physics*, 2021(3), Mar 2021.

[10] V.V. Barmin, V.G. Barylov, I.V. Chuvilo, G.V. Davidenko, V.S. Demidov, A.G. Dolgolenko, A.G. Meshkovsky, L.B. Okun, V.A. Shebanov, M. Baldo-Ceolin, E. Calimani, S. Ciampolillo, F. Mattioli, G. Miari, and A. Sconza. Cpt symmetry and neutral kaons. *Nuclear Physics B*, 247(2):293–312, 1984.

[11] Alexander Belyaev, Roshan Foadi, Mads T. Frandsen, Matti Järvinen, Francesco Sannino, and Alexander Pukhov. Technicolor walks at the lhc. *Physical Review D*, 79(3), Feb 2009.

[12] Carsten Bittrich. Evidence for Scattering of Electroweak Gauge Bosons in the $W^{\pm}Z$ Channel with the ATLAS Detector at the Large Hadron Collider, 2020. Presented 14 Jul 2020.

[13] Angela Maria Burger. Measurement of Vector Boson polarisation in WZ production at the LHC with the ATLAS detector. Mesure de la polarisation de bosons vecteurs lors de leur production par paire WZ au LHC avec le détecteur ATLAS, May 2018. Presented 03 Jul 2018.

[14] Cheng-Wei Chiang. Examining custodial symmetry in the higgs sector of georgi-machacek model. 05 2013.

[15] Wikimedia Commons. File:standard model of elementary particles.svg — wikimedia commons, the free media repository, 2021. [Online; accessed 31-May-2021].

[16] John Ellis, Mary K. Gaillard, and Dimitri V. Nanopoulos. A Historical Profile of the Higgs Boson. An Updated Historical Profile of the Higgs Boson. (KCL-PH-TH-2015-20. KCL-PH-TH-2015-20. LCTS-2015-10. CERN-PH-TH-2015-098):255–274. 20 p, Apr 2015. 22 pages, 5 figures, update of arXiv:1201.6045, to be published in the volume.

[17] Lyndon Evans and Philip Bryant. LHC machine. *Journal of Instrumentation*, 3(08):S08001–S08001, aug 2008.

[18] Benjamin Freund. Search for resonant w z production in the fully leptonic final state with the atlas detector.

[19] Howard Georgi and Marie Machacek. Doubly charged higgs bosons. *Nuclear Physics B*, 262(3):463–477, 1985.

[20] Francesco Giuli. Study of the Drell-Yan process with the ATLAS detector at the LHC, Oct 2018. Presented 09 Nov 2018.

[21] Jeffrey Goldstone, Abdus Salam, and Steven Weinberg. Broken symmetries. *Phys. Rev.*, 127:965–970, Aug 1962.

[22] Julie Haffner. The CERN accelerator complex. Complexe des accélérateurs du CERN. Oct 2013. General Photo.

[23] Kenneth Lane and Stephen Mrenna. Collider phenomenology of technihadrons in the technicolor straw man model. *Physical Review D*, 67(11), Jun 2003.

[24] Joany Manjarres Ramos. WZ Diboson Measurements with the ATLAS experiment at the LHC and Performance of resistive Micromegas in view of HL-LHC applications, 2013. Presented 08 Jul 2013.

[25] David McMahon. *Quantum Field Theory Demystified*. McGraw-Hill Professional, <country>US</country>, 2008.

[26] Vanja Morisbak. Search for New Physics with ATLAS at LHC - Z' dilepton resonance at high mass, 2010. Presented 23 Feb 2010.

[27] Yoichiro Nambu. Quasi-particles and gauge invariance in the theory of superconductivity. *Phys. Rev.*, 117:648–663, Feb 1960.

[28] Jan-Eric Nitschke. Studies on polarization in the scattering of two vector bosons withthe atlas experiment at the lhc.

[29] E. Noether. Invariante variationsprobleme. *Nachrichten von der Gesellschaft der Wissenschaften zu Göttingen, Mathematisch-Physikalische Klasse*, 1918:235–257, 1918.

[30] ATLAS Outreach. ATLAS Fact Sheet : To raise awareness of the ATLAS detector and collaboration on the LHC. 2010.

[31] Duccio Pappadopulo, Andrea Thamm, Riccardo Torre, and Andrea Wulzer. Heavy vector triplets: bridging theory and data. *Journal of High Energy Physics*, 2014(9), Sep 2014.

[32] Matthias Schott and Monica Dunford. Review of single vector boson production in pp collisions at $\sqrt{s} = 7$ TeV. Review of single vector boson production in pp collisions at $\sqrt{s} = 7$ TeV. *Eur. Phys. J. C*, 74(arXiv:1405.1160):60 p, May 2014. Comments: 60 pages, 64 figures, For Eur. Phys. J. C.

[33] M. Tanabashi, K. Hagiwara, K. Hikasa, K. Nakamura, Y. Sumino, F. Takahashi, J. Tanaka, K. Agashe, G. Aielli, C. Amsler, M. Antonelli, D. M. Asner, H. Baer, Sw. Banerjee, R. M. Barnett, T. Basaglia, C. W. Bauer, J. J. Beatty, V. I. Belousov, J. Beringer, S. Bethke, A. Bettini, H. Bichsel, O. Biebel, K. M. Black, E. Blucher, O. Buchmuller, V. Burkert, M. A. Bychkov, R. N. Cahn, M. Carena, A. Ceccucci, A. Cerri, D. Chakraborty, M.-C. Chen, R. S. Chivukula, G. Cowan, O. Dahl, G. D'Ambrosio, T. Damour, D. de Florian, A. de Gouvêa, T. DeGrand, P. de Jong, G. Dissertori, B. A. Dobrescu, M. D'Onofrio, M. Doser, M. Drees, H. K. Dreiner, D. A. Dwyer, P. Eerola, S. Eidelman, J. Ellis, J. Erler, V. V. Ezhela, W. Fetscher, B. D. Fields, R. Firestone, B. Foster, A. Freitas, H. Gallagher, L. Garren, H.-J. Gerber, G. Gerbier, T. Gershon, Y. Gershtein, T. Gherghetta, A. A. Godizov, M. Goodman, C. Grab, A. V. Gritsan, C. Grojean, D. E. Groom, M. Grünewald, A. Gurtu, T. Gutsche, H. E. Haber, C. Hanhart, S. Hashimoto, Y. Hayato, K. G. Hayes, A. Hebecker, S. Heinemeyer, B. Heltsley, J. J. Hernández-Rey,

J. Hisano, A. Höcker, J. Holder, A. Holtkamp, T. Hyodo, K. D. Irwin, K. F. Johnson, M. Kado, M. Karliner, U. F. Katz, S. R. Klein, E. Klempt, R. V. Kowalewski, F. Krauss, M. Kreps, B. Krusche, Yu. V. Kuyanov, Y. Kwon, O. Lahav, J. Laiho, J. Lesgourgues, A. Liddle, Z. Ligeti, C.-J. Lin, C. Lippmann, T. M. Liss, L. Littenberg, K. S. Lugovsky, S. B. Lugovsky, A. Lusiani, Y. Makida, F. Maltoni, T. Mannel, A. V. Manohar, W. J. Marciano, A. D. Martin, A. Masoni, J. Matthews, U.-G. Meißner, D. Milstead, R. E. Mitchell, K. Mönig, P. Molaro, F. Moortgat, M. Moskovic, H. Murayama, M. Narain, P. Nason, S. Navas, M. Neubert, P. Nevski, Y. Nir, K. A. Olive, S. Pagan Griso, J. Parsons, C. Patrignani, J. A. Peacock, M. Pennington, S. T. Petcov, V. A. Petrov, E. Pianori, A. Piepke, A. Pomarol, A. Quadt, J. Rademacker, G. Raffelt, B. N. Ratcliff, P. Richardson, A. Ringwald, S. Roesler, S. Rolli, A. Romaniouk, L. J. Rosenberg, J. L. Rosner, G. Rybka, R. A. Ryutin, C. T. Sachrajda, Y. Sakai, G. P. Salam, S. Sarkar, F. Sauli, O. Schneider, K. Scholberg, A. J. Schwartz, D. Scott, V. Sharma, S. R. Sharpe, T. Shutt, M. Silari, T. Sjöstrand, P. Skands, T. Skwarnicki, J. G. Smith, G. F. Smoot, S. Spanier, H. Spieler, C. Spiering, A. Stahl, S. L. Stone, T. Sumiyoshi, M. J. Syphers, K. Terashi, J. Terning, U. Thoma, R. S. Thorne, L. Tiator, M. Titov, N. P. Tkachenko, N. A. Törnqvist, D. R. Tovey, G. Valencia, R. Van de Water, N. Varelas, G. Venanzoni, L. Verde, M. G. Vincter, P. Vogel, A. Vogt, S. P. Wakely, W. Walkowiak, C. W. Walter, D. Wands, D. R. Ward, M. O. Wascko, G. Weiglein, D. H. Weinberg, E. J. Weinberg, M. White, L. R. Wiencke, S. Willocq, C. G. Wohl, J. Womersley, C. L. Woody, R. L. Workman, W.-M. Yao, G. P. Zeller, O. V. Zenin, R.-Y. Zhu, S.-L. Zhu, F. Zimmermann, P. A. Zyla, J. Anderson, L. Fuller, V. S. Lugovsky, and P. Schaffner. Review of particle physics. *Phys. Rev. D*, 98:030001, Aug 2018.

[34] Mark Thomson. *Modern Particle Physics.* Cambridge University Press, 2013.

[35] David Tong. David tong: Lectures on gauge theory, university of cambridge. http://www.damtp.cam.ac.uk/user/tong/gaugetheory.html.

[36] L. Wolfenstein. Neutrino masses and solar neutrinos. *Phys. Rev. D*, 45:R4365–R4366, Jun 1992.

Erklärung

Hiermit erkläre ich, dass ich diese Arbeit im Rahmen der Betreuung am Institut für Kern- und Teilchenphysik ohne unzulässige Hilfe Dritter verfasst und alle Quellen als solche gekennzeichnet habe.

Alhawiti, Fawaz Mutlaq S
Dresden, September 2021